



POLITECNICO
MILANO 1863

SCUOLA DI INGEGNERIA INDUSTRIALE
E DELL'INFORMAZIONE

Pareto Optimization and Power Electronics Realization of Orthogo- nal Field WPT Concept

TESI DI LAUREA MAGISTRALE IN
ELECTRICAL ENGINEERING - INGEGNERIA ELETTRICA

Author: **Devpriy Yadav**

Student ID: 942631

Advisor: Prof. Dr. Roberto Perini

Co-advisors: Prof. Dr. Johann Walter Kolar (PES, ETH Zurich)

Academic Year: 2020-21

Abstract

As wireless power transfer (WPT) is gaining more and more popularity in modern times, it is finding its applications in many new areas, ranging from tiny implantable medical devices to large scale EV charging infrastructure. One such area where WPT has caught attention is high purity manufacturing industries such as pharmaceuticals and semiconductor manufacturing industries, where high purity environment requirements renders the supplied equipment to be completely encapsulated in metallic/electrically conductive enclosure. Thus WPT certainly have one up in this area. However, due to presence of electrically conductive material (usually stainless steel (SS)), the alternating flux crossing it induces eddy currents which causes a part of transferred power to be lost in the SS which reduces its efficiency. Such a system to supply equipment through SS has been realized and tested.

This master thesis focuses on improving the performance of the system by geometry optimization. Different types of WPT through SS (ie. OFC and PFC) are discussed. To optimize the system, it first needs to be modelled. Various modelling techniques like Numerical, Semi-Numerical, analytic, are discussed and their complexity is analysed. Electrical as well as magnetic modelling is discussed and analytical model of OFC-WPT is developed which is later used to geometrically optimize the system.

The major factor that governs the losses on SS is its resistance, which very well depends on the system geometry. So geometrical modification, like introducing pole shoes at the limbs of e-core is proposed. The idea is backed by analytic modelling of equivalent SS resistance and finally geometry optimization is performed. Since geometry optimization has many variables, approach to use boxed volume optimization is taken. Further, the device is optimized to give 50W output power at 60V input voltage. The optimized design is realized in hardware and analytical calculations are then verified on the prototype.

Keywords: Wireless Power Transfer, Magnetic Modelling, IPT, ICWPT, WPT, Solid Losses, AC losses, optimization, boxed volume optimization.

Contents

Abstract	i
Contents	iii
1 Introduction	1
2 Fundamentals of Wireless Power Transfer	5
2.1 Inductive Power Transfer System	5
2.1.1 Transformer Equivalent Circuit	6
2.1.2 Losses in WPT	7
2.1.3 WPT through Stainless Steel	8
2.2 OFC - WPT: Modelling and Analysis	9
2.2.1 OFC-WPT Equivalent Circuit	9
2.2.2 Resonant Compensation	11
3 Model and Optimization Methods	15
3.1 OFC-WPT Model and proposed geometrical modifications	15
3.2 Optimization methods	18
3.2.1 FEM Model and optimization approach	19
3.2.2 Analytical Modelling and Optimization	21
3.3 Geometry Optimization	31
4 Hardware Implementation	37
4.1 WPT Hardware Realization	37
4.1.1 Analysis of Optimisation optimum design	37
4.1.2 WPT Module realization	38
4.2 Power Electronics for WPT	38
5 Results	43
5.1 Measurement Techniques	43

5.2	Prototype Testing	45
6	Conclusion	47
6.1	Outlook	47
6.2	Future Work	47
	Bibliography	49
	A Appendix A	51
A.1	Equations for AC constant calculations	51
A.2	Load Resistance calculation for constant 50W output power	51
	List of Figures	53
	List of Tables	57
	Acronyms	59
	Acknowledgements	61

1 | Introduction

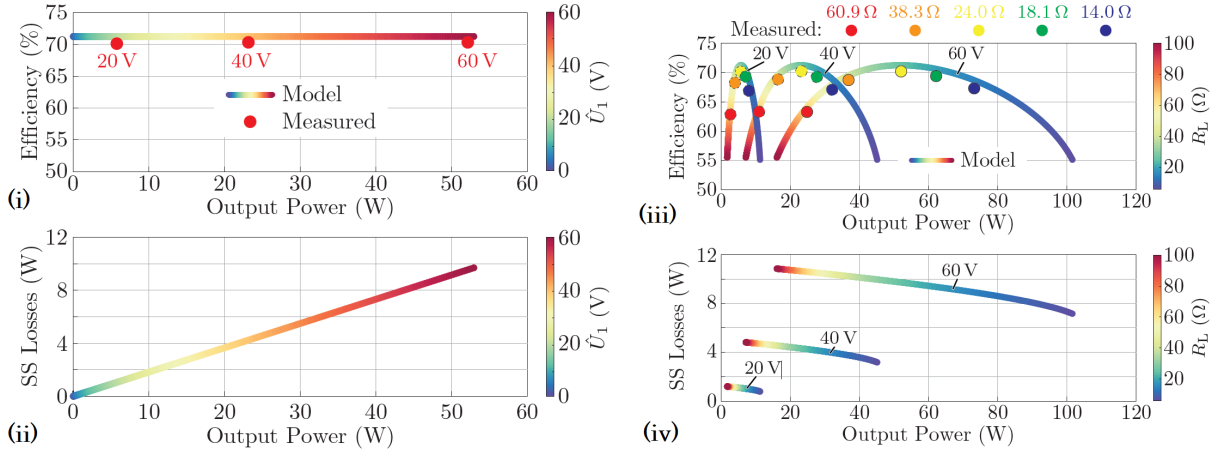
Modern Inductive Power Transfer (IPT) systems are in existence since 1960's where they found applications in biomedical and radio-frequency identification systems, mainly supplying implanted devices and for remote sensors.

IPT currently have also found applications in battery charging technology for consumer electronic devices as well as for charging the batteries of Electric or Hybrid Electric Vehicles (EV/HEV). [4]

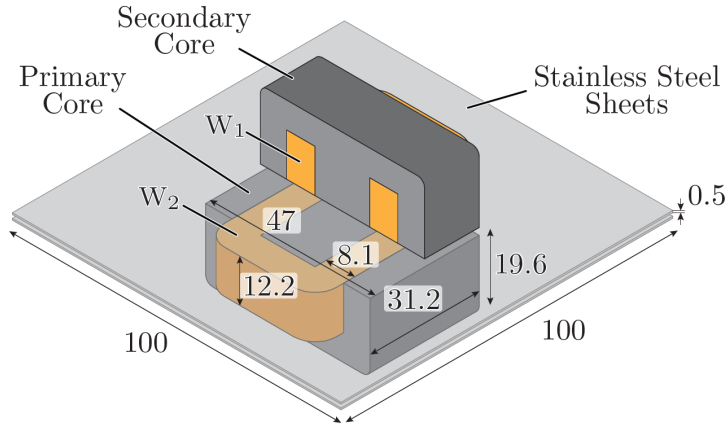
In conventionally, the WPT system primary-side and secondary-side coils are realized as air coils with litz wire, while flux guidance is provided by magnetic material suitable to be used at high frequencies, typically ferrite cores, which also offers better coupling and shielding. Use of litz wire eliminates the frequency-dependent parasitic skin and proximity effects allowing the IPT system to operate at high frequencies of the alternating field (tens of kHz, typically 85 kHz) with high transmission efficiencies of $\geq 90\%$. [10]

In high purity industries such as pharmaceutical and semiconductor industries, the manufacturing environment have very high purity environment requirement. The manufacturing units are often enclosed in Stainless Steel enclosures to ensure high purity. To supply systems inside a closed environment is usually achieved by cable carriers. This may compromise the purity of the environment. Also with time, the cables loosens due to ageing which may also cause contamination. Thus transmitting power wirelessly is a promising solution. However, due to presence of conductive material in between the sending and receiving module, usually stainless steel (SS), there are losses in SS. This limits the maximum efficiency of the WPT module.

Previously there has been work done in developing such a WPT module through SS. An MSc thesis [10] has been conducted in this topic in which different wireless power transfer methods through SS has been studied and realized in hardware. The work included modelling the differnt WPT modules (OFC and PFC), analysing equivalent circuits and realizing and testing it in hardware demonstrator. The OFC-WPT module achieved 72% of maximum efficiency at 50W output power & 60V input voltage [8]. Figure 1.1 shows the OFC-WPT model developed along with it's performance parameters.



(a) Base Design Performance:: (i): $Eff.$ vs P_{out} as a function of \hat{U}_1 , shows constant trend of efficiency over entire voltage range, (ii): SS Losses vs P_{out} as a function of \hat{U}_1 , shows linear trend, (iii): $Eff.$ vs P_{out} as a function of R_L , (iv): SS Losses vs P_{out} as a function of R_L .



(b) Base Design (All dimensions in mm)

Figure 1.1: Previous Work on OFC-WPT [8]

However, the design was not geometrically optimized. This thesis mainly focuses on geometrically optimizing the OFC-WPT module to improve the efficiency for given power, voltage and volume of the module. The base design as shown in Figure 1.1b is taken as reference and is geometrically optimized with constant boxed volume. The module is studied for developing analytical modelling, which is used to run the optimization routine. The most efficient design is chosen, realized and tested, such that it delivers 50W output power at fixed 60V input voltage operating at calculated efficiency.

Outline of the Thesis

This thesis is organized as follows: In second chapter, the fundamentals of WPT are discussed along with modelling and developing equivalent circuit of OFC-WPT module.

The Third chapter lays down ground for modifications in the base design to reduce losses and increase the efficiency. Optimisation methods are discussed and the analytical approach used for geometry optimization is developed and implemented. In chapter Four, the optimum design is selected, analysed and methods to realize it in hardware along with required power electronics to supply it are discussed. In Chapter Five we will see the tests and measurements done on the developed model and results are analysed. Finally, In Chapter Six the thesis is concluded along with a discussion on future research work in this area.

2 | Fundamentals of Wireless Power Transfer

In this chapter, the working principle of WPT and modeling of equivalent circuit for performance analysis is presented. Later, the method to evaluate analytical performance is studied.

2.1. Inductive Power Transfer System

The main objective of an IPT system is to transfer power to a moveable component across gapped magnetic structure. The complete realization of Inductively Coupled WPT system is an intricate amalgamation of magnetics and power electronics. Due to the large air gap, the magnetic coupling between primary and secondary is lower, which leads to low mutual inductance and higher leakage inductance. Because of this, the power conditioner along with circuit tuning is required for efficient operation of WPT system. The elements of the ICWPT are shown in Figure 2.1 [1].

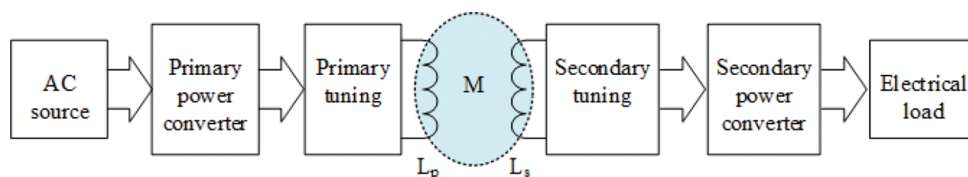


Figure 2.1: Elements of Inductively Coupled WPT system [1]

The basic principle of operation of WPT is governed by Amperé's law and Faraday's law. The working of ICWPT can be modelled and better understood by equivalent circuit of a transformer [3].

The analysis of MF transformers for Power Electronic applications can be split in various categories, such as [7]:

- **Magnetic:** The magnetizing flux, leakage flux relations can be described by magnetic equivalent circuit.

- **Electric:** Parasitics of a transformer and insulation coordination can be studied by computation of electric field.
- **Losses:** The Cu-losses in windings and Core losses can be computed by different methods established in literature. Further, for purpose of this thesis, the losses in SS-sheets is modelled by incorporating a lossy tertiary winding.
- **Thermal:** To design effective cooling system for the transformer for heat extraction, the thermal model can be developed for getting the temperature distribution.

For the purpose of this thesis, the parasitic effects and thermal considerations have been neglected. Thus, for optimization, mainly the magnetic modelling of WPT and loss calculations are studied.

2.1.1. Transformer Equivalent Circuit

The main element of a WPT system is the magnetics, as the energy transfer from primary side to the secondary side is achieved via alternating magnetic field, guided through a magnetic core. The sending and receiving modules of a WPT system can be modelled as a transformer. The main magnetic field established by the excitation source can be split into two components: **(a):** Leakage field, & **(b):** Mutual field.

An ideal transformer can be represented by two mutually coupled coils, as shown in Figure 2.2, the leakage field and mutual field can be modelled by Leakage Inductance (L_σ) and Mutual Inductance (L_μ or M) respectively. The differential equations of an ideal transformer can be described fully by 3 circuit elements, namely: Primary & Secondary Self Inductances (L_1 & L_2), and Mutual Inductance (L_μ or M).

$$\begin{aligned} u_1 &= L_1 \frac{di_1}{dt} - M \frac{di_2}{dt} \\ u_2 &= L_2 \frac{di_2}{dt} - M \frac{di_1}{dt} \end{aligned} \quad (2.1)$$

This transformer model can be extended to any arbitrary ‘n’ value as shown in Figure 2.2. The equation. 2.1 is still valid. By choosing appropriate value of ‘n’, such as $n = k\sqrt{L_1/L_2}$, the model can be again reduced with 3 variables, where k represents the coupling coefficient of the two windings, and by definition is given by:

$$k = \frac{M}{\sqrt{L_1 L_2}} \quad (2.2)$$

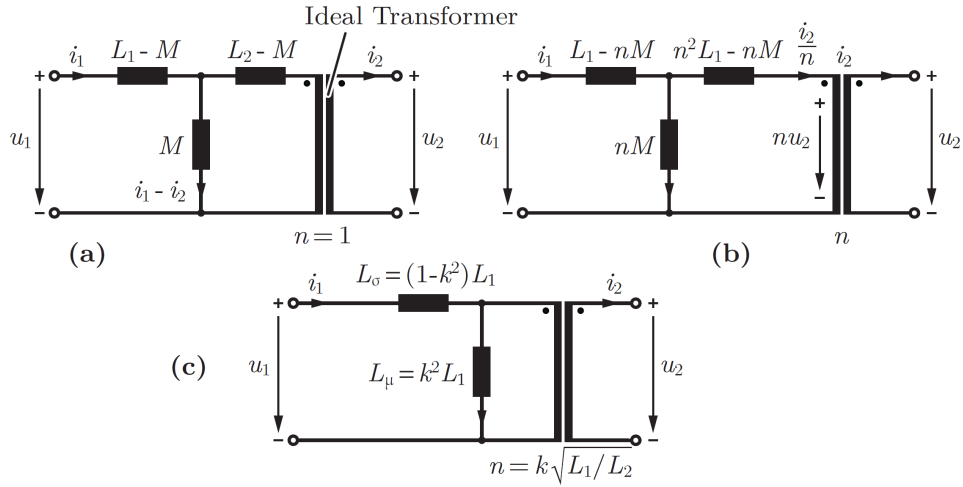


Figure 2.2: Equivalent circuit of an ideal transformer: **(a)**: Ideal transformer with $n = 1$, **(b)**: Ideal transformer with $n \neq 1$, **(c)**: Ideal transformer with $n = k\sqrt{L_1/L_2}$; [3]

2.1.2. Losses in WPT

The main loss components associated with a WPT are: **(a)**: Conduction losses in the winding of transformer **(b)**: Core losses inside magnetic material of transformer, & **(c)**: Losses associated with shielding or conductive materials present (if any).

The Cu-losses in the winding are ohmic losses due to the resistance of the winding. This resistance is frequency dependent due to the so called HF skin and proximity effects. The calculation methods of HF losses are well described in literature, and which are explained in later chapters.

The core losses in the magnetic material are due to the changing magnetic field. the three main components constituting to the core loss are: **(a)**: Hysteresis losses, **(b)**: Eddy-current core losses, & **(c)**: Residual losses. [9]

Empirically, the core loss can be characterized by the so called Steinmetz Equation (SE):

$$P_c = kf^\alpha \hat{B}^\beta \quad (2.3)$$

Where: \hat{B} is the peak flux density inside the core, f is the excitation frequency, k , α , β are material parameters.

The above equation is valid for sinusoidal excitation with DC permeabilization effect neglected. However, the excitation with power electronic systems is not always sinusoidal. For an arbitrary waveform, improved version of SE called improved Generalized Steinmetz

Equation (iGSE) can be used. For the purpose of this thesis, as the applied excitation to WPT is quite sinusoidal due to capacitive compensation (explained later), SE equation is sufficient to estimate core losses in magnetic material.

To complete the equivalent circuit of the transformer including losses, the Cu-losses are modelled as series resistance of winding, while the solid losses are represented as an equivalent solid loss resistance (R_c) in parallel with magnetization branch. The complete equivalent circuit is shown in Figure 2.3.

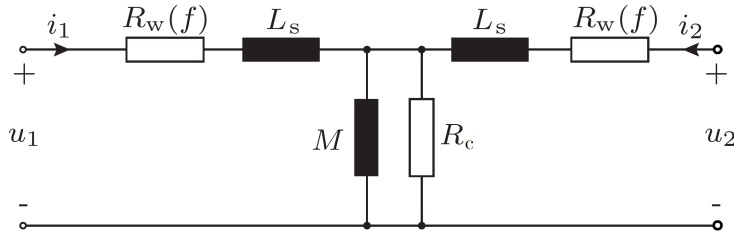


Figure 2.3: Equivalent circuit of an a real transformer including loss components. [8]

2.1.3. WPT through Stainless Steel

The conventional WPT systems employ primary and secondary coils which are generally realized as air coils. To avoid parasitic effects, litz wire is typically employed and the core is generally realized with ferrite materials. Since the HF parasitic effects are absent, high efficiencies at relatively higher frequency range can be achieved.

In high purity environments, such as Pharmaceutical or Semiconductor manufacturing industries, the equipment supplied needs to be encapsulated to avoid exposure to outside environment. These machines are usually fully enclosed by SS. The usual method of power delivery is via cable or cable carriers, which makes it challenging to seal the enclosure completely and may compromise the purity of manufacturing environment. Therefore, power transfer through wireless methods is a promising solution. However, this method has its own problems: Since SS is electrically conductive, the alternating field penetrating through it induces eddy currents. This creates additional losses and also limits the operating frequency.

The two main types of WPT methods employed through SS are: **(a)**: Parallel Field WPT Concept (PFC-WPT), & **(b)**: Orthogonal field WPT concept (OFC-WPT), depending on the way the magnetic field penetrates the SS.

As the name suggests, in PFC-WPT, the magnetic field penetrating the SS is parallel to the SS sheets, while in OFC-WPT, the magnetic field and SS sheets are orthogonal to

each other. Figure 2.4 gives a pictorial depiction of the two WPT concepts through SS. [[8, 10]]

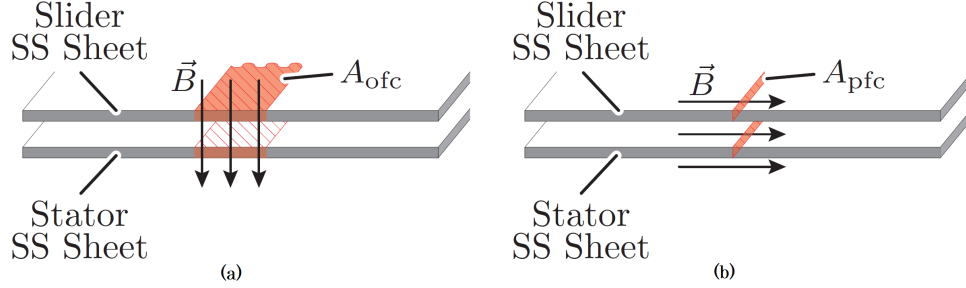


Figure 2.4: WPT Concepts through SS: (a): Orthogonal Field Concept (OFC) - \vec{B} & SS sheets are orthogonal, & (b): Parallel Field Concept (PFC) - \vec{B} & SS sheets are parallel

2.2. OFC - WPT: Modelling and Analysis

The main focus of thesis is on OFC-WPT. As seen in section 2.1.3, the magnetic field lines cross the SS sheets orthogonally. The WPT module is realized on a ferrite E-core structure, one for each: sending and receiving end. The module is supplied to the sending end winding via a DC-AC converter. This sets up the alternating magnetic field in the core which crosses the air gap, through the SS sheets, and closes through the receiving end module. This mutually coupled flux induces voltage in the secondary winding. The secondary side is connected to the load through a diode bridge.

In this chapter, we will see the equivalent circuit modelling of the OFC-WPT, concepts of resonant compensation, fundamental frequency analysis of the load and power output relation and proposed modifications to improve the efficiency of the module.

2.2.1. OFC-WPT Equivalent Circuit

The OFC-WPT is modelled as a 3-winding transformer [8] with SS sheet modelled as single turn, short-circuited winding. The equivalent circuit of the OFC-WPT is shown in Figure 2.5(b). KVL can be applied and equations can be written for the three windings as shown in Equation set 2.4.

$$\begin{aligned}
 u_1 &= R_1 i_1 + L_1 \frac{di_1}{dt} + M_{12} \frac{di_2}{dt} + M_{31} \frac{di_3}{dt}, \\
 u_2 &= R_2 i_2 + L_2 \frac{di_2}{dt} + M_{12} \frac{di_1}{dt} + M_{23} \frac{di_3}{dt}, \\
 0 &= R_3 i_3 + L_3 \frac{di_3}{dt} + M_{23} \frac{di_2}{dt} + M_{31} \frac{di_1}{dt},
 \end{aligned} \tag{2.4}$$

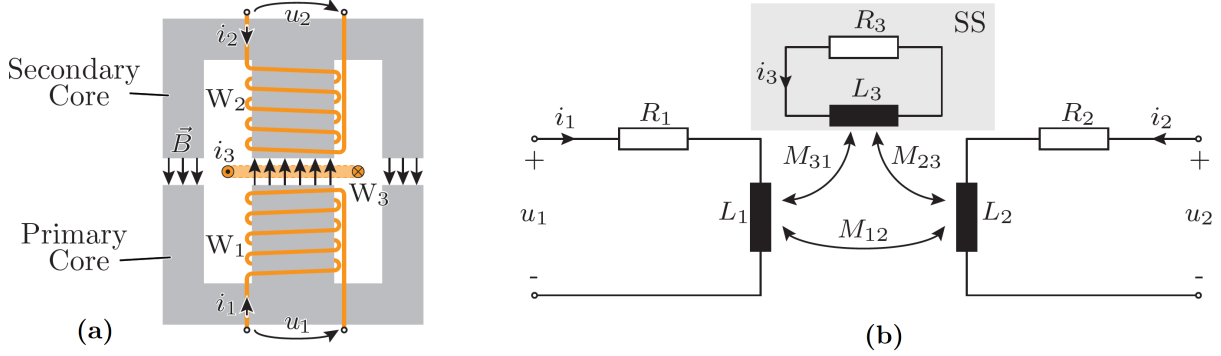


Figure 2.5: Equivalent circuit model of OFC-WPT

The mutual inductances are related to each other by no. of turns (N_1 , N_2 & N_3) as:

$$M_{12} = N_1 N_2 \cdot M_0 \quad M_{23} = N_2 N_3 \cdot M_0 \quad M_{31} = N_3 N_1 \cdot M_0 \quad (2.5)$$

where M_0 is the mutual inductance per turn. If we define turns ratio as: $n = N_1/N_2$ & $m = N_1/N_3$, the equations 2.4 can be further simplified to:

$$\begin{aligned} u_1 &= R_1 i_1 + L_1 \frac{di_1}{dt} + \underbrace{nM_{12}}_{=M} \frac{d\frac{i_2}{n}}{dt} + \underbrace{mM_{31}}_{=M} \frac{d\frac{i_3}{m}}{dt}, \\ nu_2 &= n^2 R_2 \frac{i_2}{n} + n^2 L_2 \frac{d\frac{i_2}{n}}{dt} + \underbrace{nM_{12}}_{=M} \frac{di_1}{dt} + \underbrace{nmM_{23}}_{=M} \frac{d\frac{i_3}{m}}{dt}, \\ 0 &= m^2 R_3 \frac{i_3}{m} + m^2 L_3 \frac{d\frac{i_3}{m}}{dt} + \underbrace{nmM_{23}}_{=M} \frac{d\frac{i_2}{n}}{dt} + \underbrace{mM_{31}}_{=M} \frac{di_1}{dt}, \end{aligned} \quad (2.6)$$

Since using Equations 2.5, we can simplify the mutual inductances as:

$$n M_{12} = m M_{31} = nm M_{23} = N_1^2 M_0 = M.$$

Rearranging the equations 2.6 and further simplifying, we can get:

$$\begin{aligned} u_1 &= R_1 i_1 + (L_1 - M) \frac{di_1}{dt} + M \frac{d}{dt} \left(i_1 + \frac{i_2}{n} + \frac{i_3}{m} \right), \\ nu_2 &= n^2 R_2 \frac{i_2}{n} + (n^2 L_2 - M) \frac{d\frac{i_2}{n}}{dt} + M \frac{d}{dt} \left(i_1 + \frac{i_2}{n} + \frac{i_3}{m} \right), \\ 0 &= m^2 R_3 \frac{i_3}{m} + (m^2 L_3 - M) \frac{d\frac{i_3}{m}}{dt} + M \frac{d}{dt} \left(i_1 + \frac{i_2}{n} + \frac{i_3}{m} \right). \end{aligned} \quad (2.7)$$

This equivalent circuit (Figure 2.6) is similar to the equivalent circuit of a transformer, as seen in Section 2.1 (Figure 2.3). The only addition is a parallel branch with magnetization inductance, which denotes the equivalent referred inductance of SS sheet and loss components of SS. Based on the equation set 2.7, the parameters of this OFC-WPT can be obtained from Z-parameters as [8]:

$$\begin{aligned}
 R_0 &= \Re(\underline{Z}_{11} - \underline{Z}_{12}) \\
 L_{s0} &= \Im(\underline{Z}_{11} - \underline{Z}_{12})/\omega, \\
 M_0 &= 1/\Im(1/\underline{Z}_{12}^*) \cdot 1/\omega, \text{ \&} \\
 R_3 &= 1/\Re(1/\underline{Z}_{12}^*).
 \end{aligned}
 \tag{2.8}$$

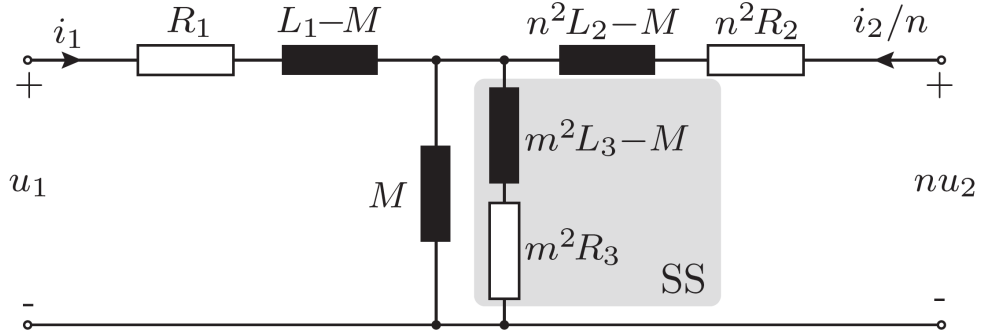


Figure 2.6: Complete equivalent circuit of OFC-WPT through SS

2.2.2. Resonant Compensation

As explained in Section 2.1, the coupling coefficient of ICWPT is quite low as coupling coefficient k is very small due to the presence of large air gap. Additionally, the presence of SS plates in OFC-WPT also, creates its own magnetic field due to eddy currents induced in it, which further reduces the coupling factor.

This low coupling factor results in relatively large voltage drops across the stray inductances, thus limiting the reduce its power transfer capability to the load. To cope with this, resonant compensation becomes necessary to achieve higher transmission efficiencies. Various compensation techniques are studied for IPT systems. The most common typologies as given in [11] are: **(a)**: Series-Series, **(b)**: Series-Parallel, **(c)**: Parallel-Series, & **(d)**: Parallel-Parallel. Figure 2.7 shows various compensation topologies.

Typically for IPTs, the receiver side is compensated with a resonant capacitor C_2 connected either in series or parallel. On transmitter side, another resonant capacitor C_1 is connected to the transmitter coil L_1 for reducing the power requirements of the converter.

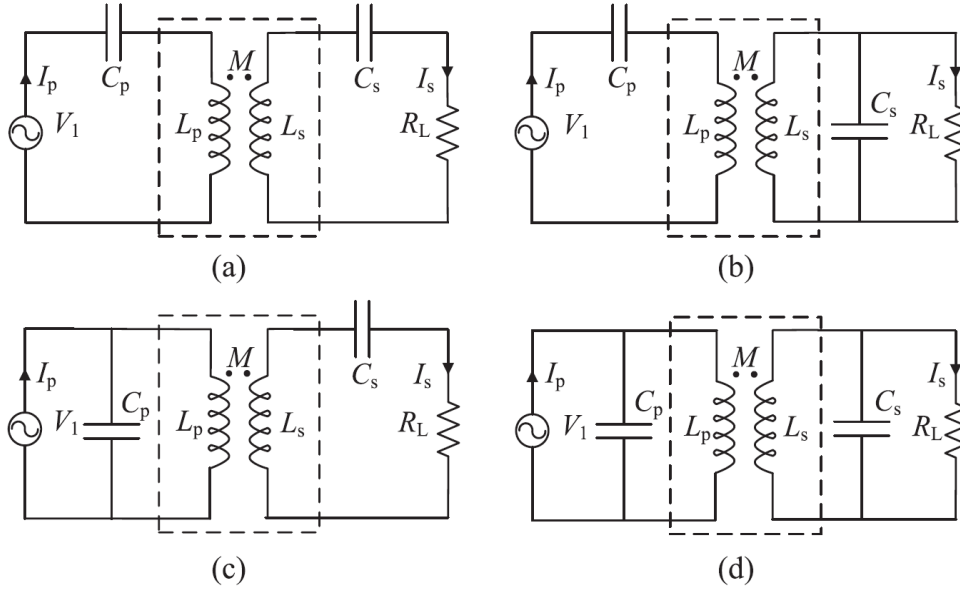


Figure 2.7: Compensation Networks for IPT: (a): Series-Series, (b): Series-Parallel, (c): Parallel-Series, & (d): Parallel-Parallel. [11]

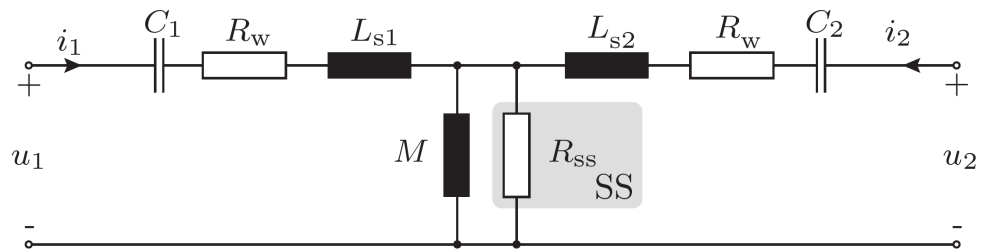
With this, we can make the phase angle of the input impedance of the resonant circuit as seen by the transmitter-side power converter to zero at the resonant frequency. And so, power converter only processes the active power required at resonant frequency, which is often same as the operating switching frequency f_{sw} . Transmitter coil can also be compensated by parallel compensation, but it requires an additional inductor connected in series between the resonant tank and the power converter. [5].

For this thesis, Series-Series Compensation technique is used. For this, usually the primary and secondary side compensation capacitances are chosen to compensate the primary and secondary self-inductances respectively at switching frequency. However, due to presence of SS, losses are larger if self-inductances are compensated as compared to only compensating leakage inductances. Therefore, for compensation, only leakage/stray inductances are compensated. After compensation, the OFC-WPT equivalent circuit can be simplified as shown in Figure 2.8.

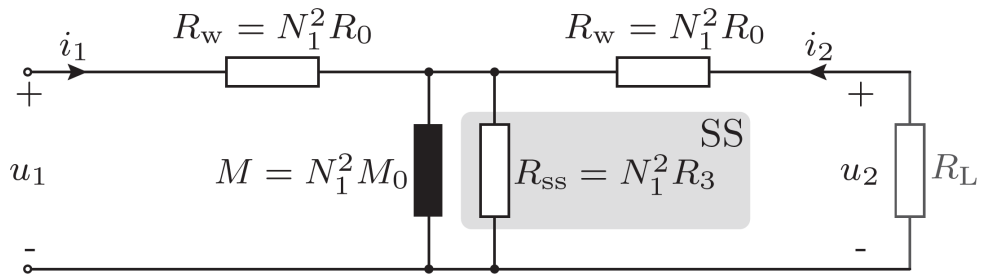
The compensation capacitors are calculated as:

$$C_1 = \frac{1}{\omega^2 L_{s1}} \quad \text{and} \quad C_2 = \frac{1}{\omega^2 L_{s2}}. \quad (2.9)$$

where $\omega = 2\pi f_{sw}$.



(a) OFC-WPT Equivalent circuit with series-series compensation.



(b) Simplified equivalent circuit

Figure 2.8: Series Compensated Equivalent circuit of OFC-WPT

3 | Model and Optimization Methods

In this chapter we will see the proposed modifications in the OFC-WPT geometry to improve its performance and effect of geometrical parameters on different circuit as well as operational parameters. later the optimization methodologies would be discussed and we will then see the modelling of system in FEM as well as Analytical environments. We would also see the methods to evaluate/estimate equivalent circuit parameters and based on that, the estimation of module performance.

3.1. OFC-WPT Model and proposed geometrical modifications

As discussed in previous chapter, the OFC-WPT module is realised with an E-type ferrite core. The main geometrical parameters as well as the physical arrangement of WPT cores can be seen in Figure 3.4. As can be seen, the magnetic flux passes from the transmitter module inside the core, through the air gap and crossing the SS sheets and finally closing through the receiving module core. It can be evaluated using Amperé law that the induced EMF in SS sheets will be maximum in the air gap between the limbs of the core. Figure 3.1 shows the distribution of induced EMF as a function of distance along the center line of SS sheet.

This will cause the eddy current to flow in the SS sheets and thus, there will be losses associated with the SS sheets. Figure 3.2 shows the distribution of Eddy current density in the SS sheet. This loss component is reflected as an equivalent resistance R_3 in the equivalent circuit of the winding model of SS (see Figure 2.5). In the simplified equivalent circuit, this equivalent SS resistance is represented by R_{SS} (see Figure 2.8).

As can be seen in the figures above, the induced EMF and thus the eddy currents are mainly induced in the air gap between the limbs of the E-core. The induced current density is maximum in the slit between the limbs of E-core (see Figure 3.2), and thus, this

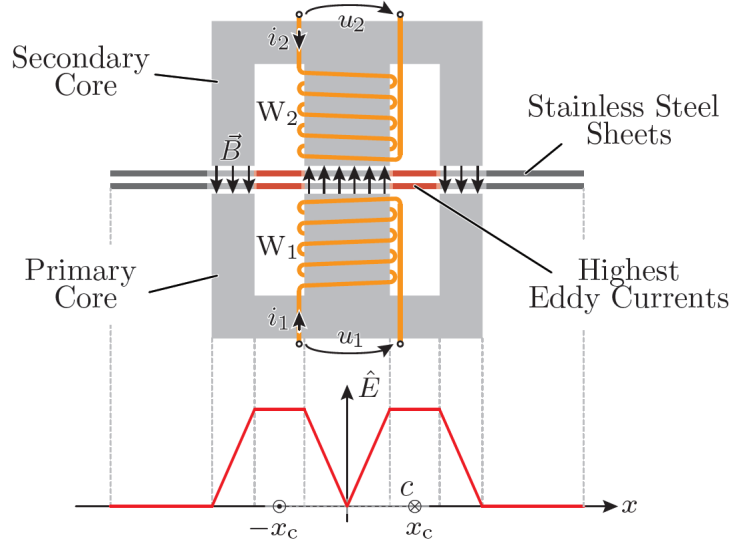


Figure 3.1: Induced EMF distribution for an E-core type OFC WPT module

section contributes to the maximum resistance to the induced eddy currents. Moreover, the induced EMF and thus the current density can be approximated to have trapezoidal distribution as shown in Figure 3.1 & Figure 3.2.

Proposed Modifications:

Since R_{SS} contributes towards maximum reduction of losses in SS, increasing the value of R_{SS} would reduce losses in SS, and thus increasing the overall efficiency of the module. As seen in Figure 3.2, the current density is maximum in the slit between the core limbs, and thus it contributes maximum to R_{SS} , since the current spreads out in the SS sheet in the area outside the slit, thus, reducing the width of this slit may increase the R_{SS} . Figure 3.3 shows the proposed modifications.

To achieve this, Pole Shoes can be introduced at the ends of the limbs to reduce the overall width of the air-gap. This would in turn reduce the cross sectional area of the eddy current path and thus increasing R_{SS} . Different Pole shoe shapes were first analysed in the FEM environment to see which pole shoe placement is best (see Figure 3.3). From the results, it was found that Pole Shoes placed symmetrically inside the air-gap gives best results with symmetric magnetic field distribution (as shown in Figure 3.3(b)).

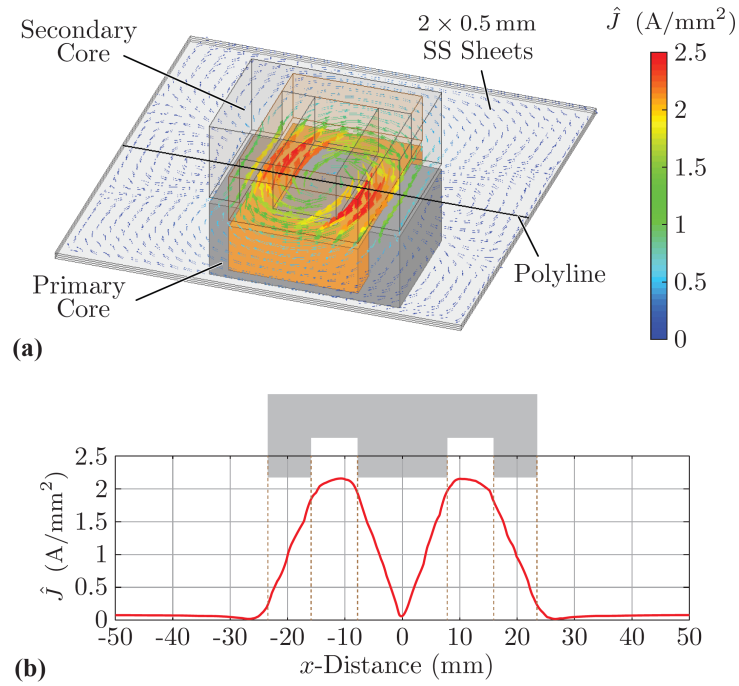


Figure 3.2: Induced Eddy Current distribution for an E-core type OFC WPT module along the center line of SS sheets.

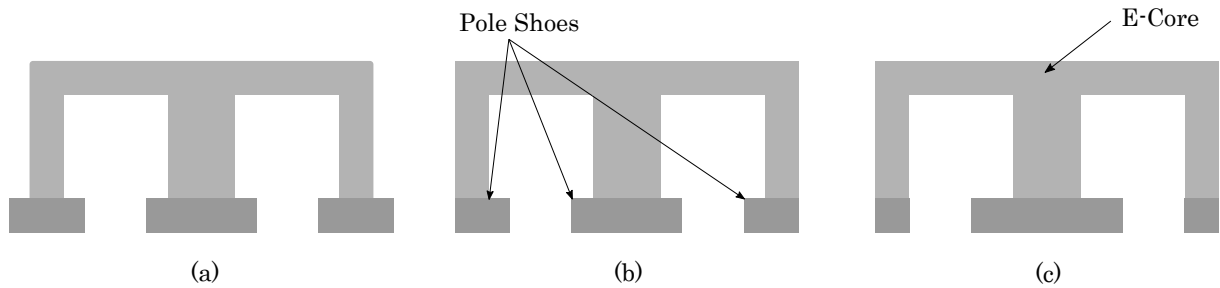


Figure 3.3: Pole Shoe Types explored:: (a): Pole Shoes placed at the center of each limb with equal pole width on each side, (b): Pole shoes placed symmetrically to get symmetric gap between the pole shoes, (c): Pole shoes placed on central limb to increase distance between air-gaps.

The details of geometrical dimensions are shown in Figure 3.4. The description of various geometrical dimensions involved is given in Table 3.1

Table 3.1: Description of Geometrical Dimensions

l_c : Core length	h_c : Core height
w_c : Core width	t_c : Core limb thickness
w_w : Winding width	h_w : Winding height
l_w : Winding length	g_{ps} : Pole shoe gap
h_{ps} : Pole shoe height	A_c : Core Area ($t_c \cdot l_c$)
A_w : Winding window area ($h_w \cdot w_w$)	x_c : Core aspect ratio (l_c/t_c)
w_{ps} : Poles shoe width	

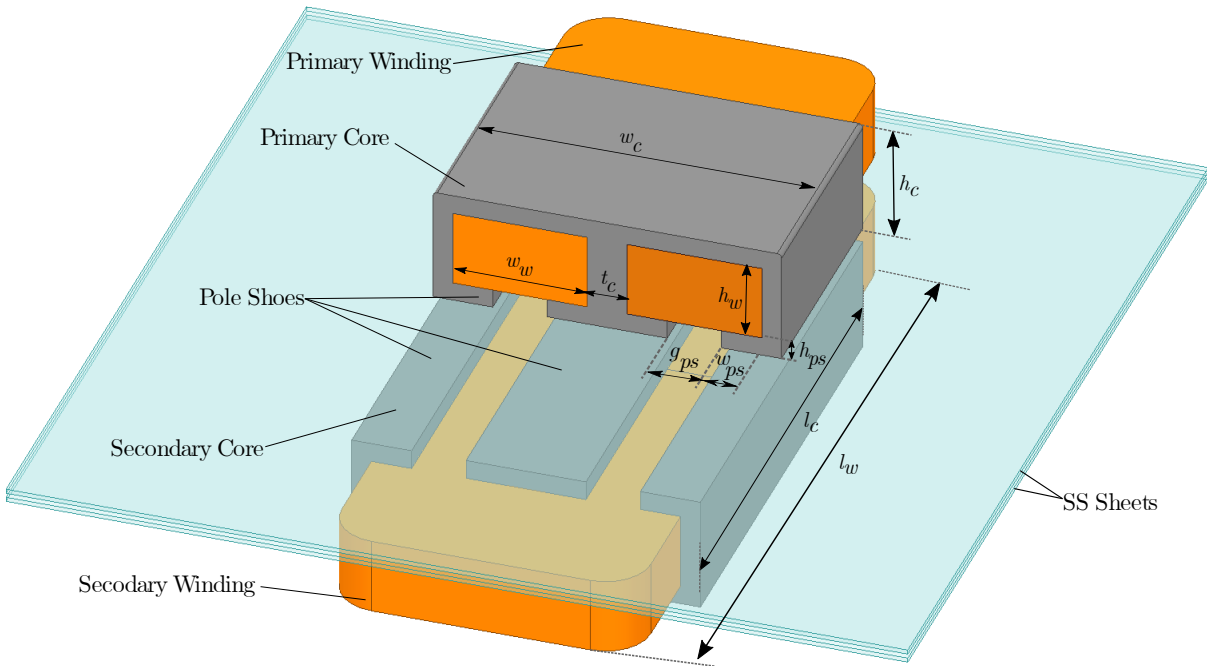


Figure 3.4: Geometrical Dimensions of OFC-WPT Module

3.2. Optimization methods

In previous chapter we have seen the geometrical model of the OFC-WPT module and also the proposed modifications in the geometry to improve performance. The main aim of this modification is to reduce the losses in the SS sheets. However, there are many other parameters which also affect the efficiency, for e.g. Switching Frequency (f_{sw}), No. of turns (N_t), Input Voltage (\hat{U}_{in}) etc.

To find the best performing parameters, we must perform an optimization routine. The output of this optimization should give the set of all the parameters (geometrical as well as operational) which would give us maximum efficiency for the module. In order to start optimization, the system needs to be modelled based on the analysis type as discussed in

Section 2.1. There are various ways to obtain the full-model of a system for optimization, classified in three categories [6]:

- **Numerical Model:** The WPT module parameters are calculated from numerical field simulations (FEM). This method is the most accurate but is very complex and time-consuming.
- **Semi-Numerical models:** The model is derived using analytical equations, but doesn't have an explicit solution. Optimized design is found through numerical optimizations, but is difficult to realize mechanism leading to optimized design. Reasonably fast compared to Numerical Model.
- **Fully Analytical:** Closed form solution analytical equations of the model are used. Simple, fast but accuracy of this method is limited.

For the purpose of this thesis, FEM model and Fully - Analytical Models are used. Initially, the FEM approach was used to get the model parameters, and then optimization was run in MATLAB program. This optimization method was kept unconstrained and all the parameters were varied. This resulted in getting most optimum designs at the extremes of the design space. This approach was therefore not suitable, hence analytical model was developed and optimization was run with fully analytical model in MATLAB. Both the optimization methods are discussed in detail in next sections.

3.2.1. FEM Model and optimization approach

To assess performance of the module, the equivalent circuit as shown in Figure 2.8 is used and the circuit parameters needs to be known. The model parameters of such a circuit can be extracted from its Z-parameters (ref: Equation 2.8).

In FEM environment, the physical model can be created and analysed for different frequencies and excitation types for optimization. From the analysis results, various parameters such as Z-parameters, Field Distribution, loss calculations etc. can be evaluated. For our analysis, we would need the Z-parameters to obtain circuit parameters. The model is parameterized and controlled externally through a MATLAB program. The geometrical parameters are iteratively varied to solve for different geometries of WPT. For each geometry, the analysis data is exported and is then processes in a separate program in MATLAB. Based on the filtering criteria, invalid design are discarded and Pareto Plots are generated to observe the efficiency trends. The complete working flowchart for FEM based optimization approach is shown in Figure 3.5.

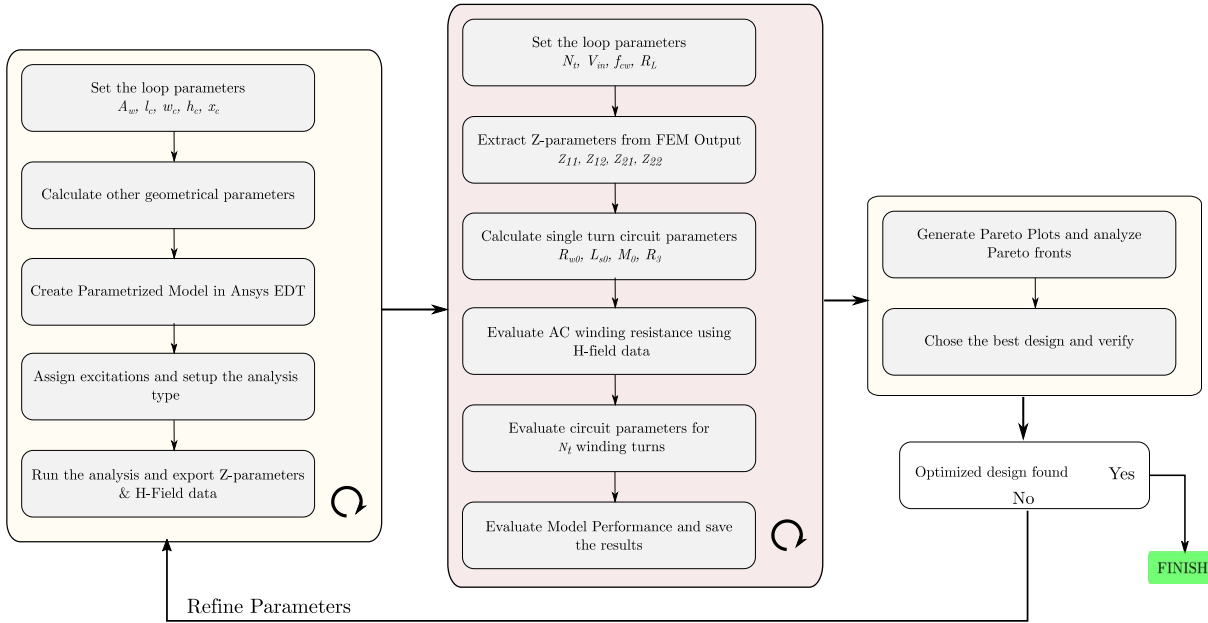


Figure 3.5: FEM Optimization Flowchart

A typical workflow of modelling in FEM environment is shown in Figure 3.7. Parametrized commands generates the geometry in Ansys EDT, solves analyses the model and saves the analysis results.

After processing the FEM data, a typical $\eta - \rho$ Pareto plot is obtained as shown in Figure 3.6. The plots can be generated as a function of different geometrical as well as operational parameters. As can be seen in Figure 3.6, the design space for all the valid designs in plotted as a function of f_{sw} , $g_{ps(pu)}$, l_c & A_c , with all the variables free no clear trend is discernible. Therefore, some parameters needs to be fixed.

A design from the pareto plot can be chosen and can be verified back in Ansys with actual excitation, i.e. a solid single turn winding replaced with actual winding. The winding can be modelled in Ansys Maxwell circuit and excited with actual voltage source to verify the actual performance which was previously calculated analytically in MATLAB using Z-parameters.

From the analysis, the fields plots can also be generated to verify the peak flux densities in the core and current densities in the windings. Figure 3.8 shows a typical field distribution plot obtained from FEM analysis. This tool is helpful in checking for any saturation effects in the core, or to see the maximum current densities to observe any thermal considerations.

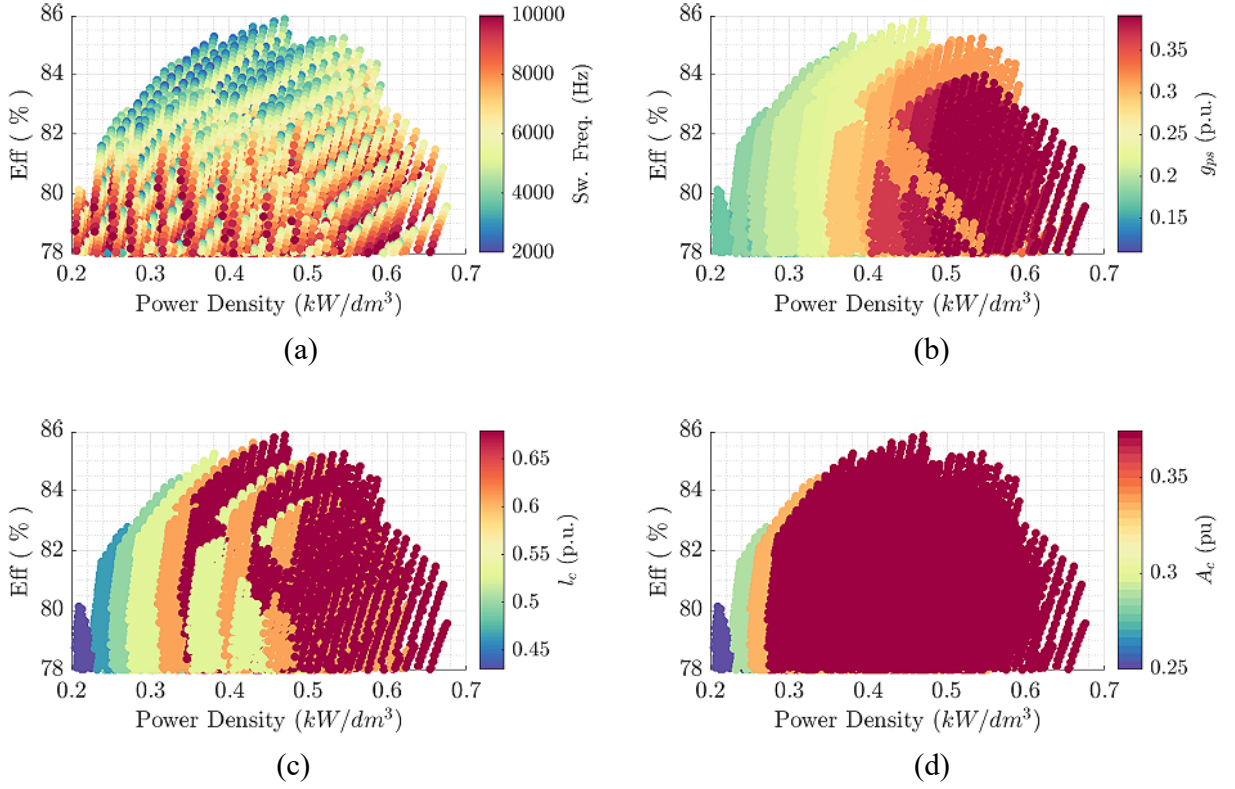


Figure 3.6: $\eta - \rho$ Pareto Plot for FEM based optimization analysis, with filtering criteria applied as:- $\hat{B}_{pk} \leq 0.3T$, $d_{wire} \leq 1mm$, $\hat{J}_{pk} \leq 5A/mm^2$ & $\eta \geq 78\%$.

3.2.2. Analytical Modelling and Optimization

In Section 3.2.1 we saw the Numerical method of optimization. Though accurate, this method is computationally intensive and time consuming. Since there are many parameters involved in the geometry optimization, a good approach will be to analyse the model in fully-analytic way.

To do that, the different circuit elements namely R_w , L_s , M , & R_{SS} (Figure 2.8) needs to be modelled individually. These parameters are linked with geometrical as well as operational parameters. Thus, the analytical closed form equations needs to be developed which links the operational & geometrical parameters with the circuit parameters. After obtaining closed form equations, the optimization routine similar to FEM approach can be run to find the optimized design. The modelling methods of circuit elements are discussed in detail in following sections.

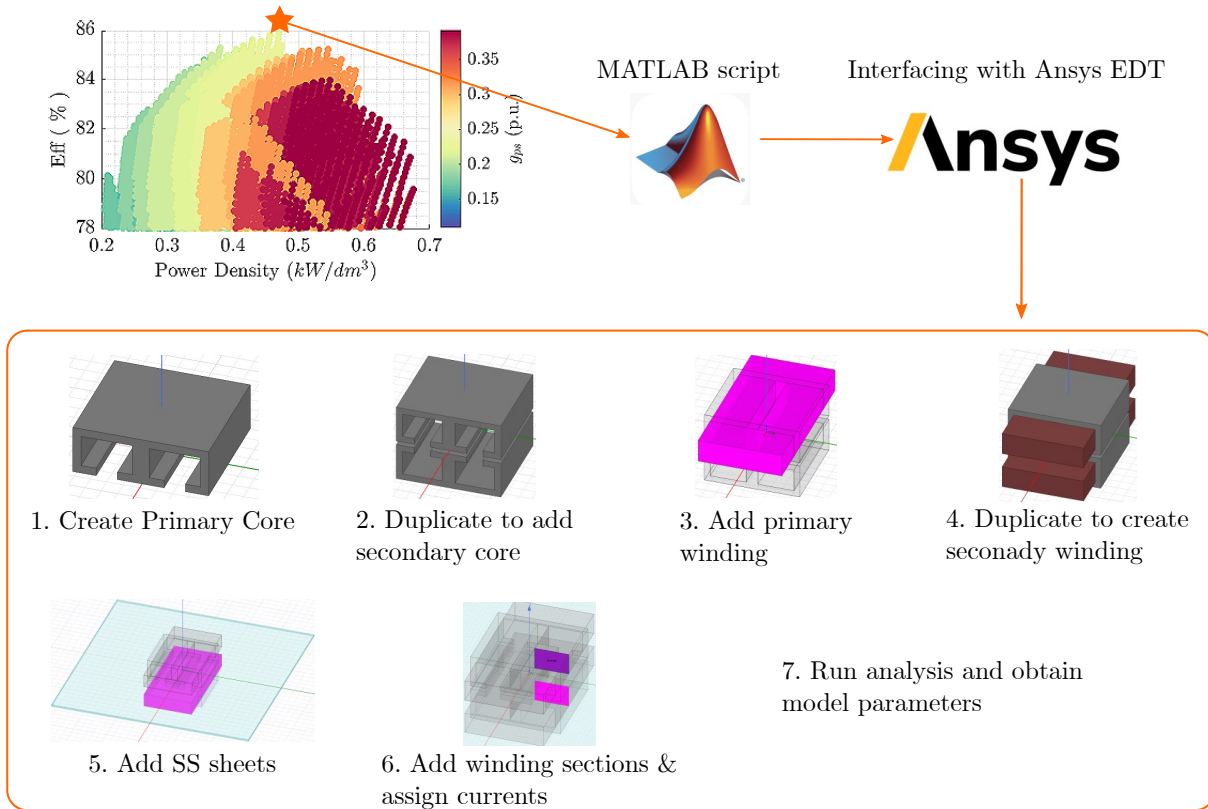


Figure 3.7: FEM Workflow

Magnetic Modelling of OFC-WPT module

The main component of the OFC-WPT is the E-core, and the magnetics play a pivotal role in determining the performance. The magnetic modelling of the E-core is to be done to determine the flux linkage of the transmitter module with the receiver module. The mutual flux linked with primary (transmitting side) and secondary (receiving side) mainly contributes to the power transfer. However, not all the flux that is generated in the primary module links with the secondary side. Some flux lines close through the air within the primary (or secondary) modules, which is called the *Leakage Flux*.

As was seen in Section 2.1.1, the two flux fields: *Leakage* & *Mutual* fluxes can be modelled as Inductances, namely: *Leakage* (L_σ) & *Mutual* (M or L_μ) Inductance respectively. Referring to the equivalent circuit of the OFC-WPT (Figure 2.8), the primary and secondary sides have their respective leakage inductances (L_σ). The mutual inductance (M) takes into account the flux linked with Primary & Secondary and also the flux linked with SS sheets.

The magnetic circuit modelling of the WPT is analogous to modelling electric circuit. Just like KVL for electric circuits, the Amperé's Law states that sum of magnetomotive

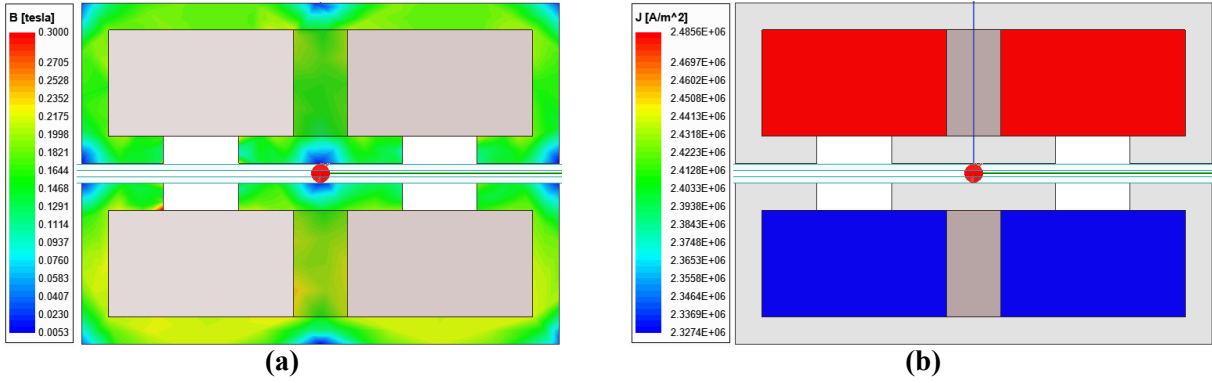


Figure 3.8: Field Plots of FEM analysis:: (a): Flux density distribution inside the core, (b): Current density distribution inside the windings

force (MMF) in a closed loop is zero and similar to KCL, the Gauss' law for magnetic circuit states that sum of magnetic flux at a node is zero. Similar to resistance in electric circuits, the resistance of flow of magnetic flux is defined as *Reluctance*: $R_m = MMF/\phi$. Hence the magnetic model is also simply called the *Reluctance Model*. [9]

Using the reluctance model, the inductance of any inductive components having N_t turns of winding and total reluctance $R_{m,tot}$ can be evaluated as:

$$L = \frac{N_t^2}{R_{m,tot}} \quad (3.1)$$

To get the inductance, we must first know the reluctance of each section of the inductive component. The OFC-WPT module thus can be divided into different sections as shown in Figure 3.9(a). For each section, the reluctance can be calculated as:

$$R_m = \frac{l}{\mu_0 \mu_r A_{cm}} \quad (3.2)$$

where R_m is the reluctance of the path/section, l is the length of the section, A_{cm} is the cross sectional area of the magnetic material section and $\mu_0 \mu_r$ is the permeability of the section ($\mu_r = 1$ for air). [9]

Referring to Figure 3.9(a), the reluctances R_1 , R_2 & R_4 are the reluctances of the magnetic material, while reluctances R_3 , R_5 & R_6 are reluctances in the air path. The reluctance R_3 & R_5 contributes to the leakage inductances. The various dimensions in calculation of reluctances is given in the Table 3.2, where μ_r is the relative permeability of N86 Ferrite material, μ_0 is the permeability of air, g_a is the air gap between primary and secondary cores and other geometrical dimensions as described in Table 3.1.

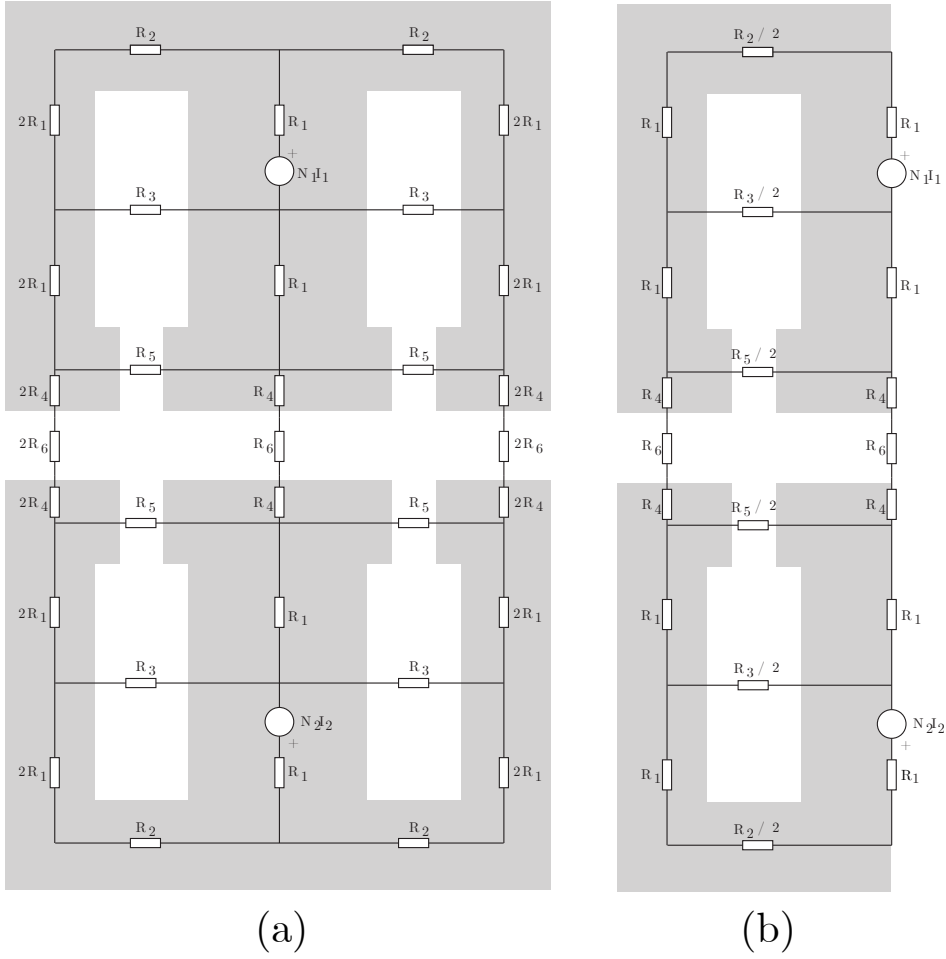


Figure 3.9: Magnetic modelling of OFC-WPT module:: (a): E-core split into different sections and reluctances calculated for for each section, (b): Reluctance model simplified along the central symmetry axis.

Using symmetry, the reluctance network shown in Figure 3.9(a) can be simplified to that shown in Figure 3.9(b) & Figure 3.10(a). This is a typical ladder network which can be reduced to an equivalent-T network as shown in Figure 3.10(b). From this, the total flux ϕ_1 can be split into the mutual flux ϕ_m and leakage flux ϕ_{s1} . Using this, we can calculate the inductances as:

$$L_{s1} = \frac{N_1 \phi_{s1}}{I_1} \quad \& \quad L_{mu} = \frac{N_1 \phi_{mu}}{I_1} \quad (3.3)$$

SS Resistance Calculation

As discussed in Section 2.2, the alternating flux generated by exciting the primary winding, crosses the SS sheets orthogonally in OFC-WPT. This alternating flux induces eddy

Reluctance	l	A_{cm}	μ
R_1	$h_w + \frac{t_c}{2}$	$l_c \cdot t_c$	$\mu_0\mu_r$
R_2	$w_w + \frac{3t_c}{4}$	$\frac{l_c \cdot t_c}{2}$	$\mu_0\mu_r$
R_3	w_w	$w_h \cdot l_c$	μ_0
R_4	$\frac{h_{ps}}{2}$	$(2w_{ps} + t_c) \cdot l_c$	$\mu_0\mu_r$
R_5	g_{ps}	$h_{ps} \cdot l_c$	μ_0
R_6	g_a	$(2w_{ps} + t_c) \cdot l_c$	μ_0

Table 3.2: Parameter description for calculation of reluctance model.

currents in the SS sheets and contributes to solid losses. These losses can be modelled as an equivalent resistance R_{SS} as shown in the equivalent circuit of OFC-WPT (Figure 2.8). From the Equations 2.7, we can see that R_{SS} can be written as (ref. Figure 2.8(b)):

$$R_{SS} = N_t^2 \cdot R_3 \quad (3.4)$$

where N_t is the number of winding turns and R_3 is the single turn SS resistance. Since N_t is known quantity, we need to model R_3 to get the value of R_{SS} .

We had already seen previously that the induced eddy currents mainly flows in the slit between the core limbs. This can be seen clearly in Figure 3.11 that this portion of SS (R_1) contributes mainly towards the total resistance in R_3 , as the eddy currents can spread in wider area outside this region and thus the resistance of this region (R_2) is quite lower as compared to the section of SS directly below the slit. Moreover, it is quite difficult to estimate the total resistance in the region outside the slit, so empirical methods are used to correct for the resistance value.

We had seen previously in Section 3.1 (Figure 3.2) that the current density is maximum in the slit area and has more of a trapezoidal distribution (ref. Figure 3.11). Thus, for our analysis, we can approximate a trapezoidal cross-section of SS sheet directly below the slit region for calculation of SS resistance in this region. Figure 3.11(b) & 3.11(c) shows the current density distribution approximation and the dimensions involved.

The effective width of the SS sheet therefore can be approximated as shown in Figure 3.11(b). Therefore, for the region below the slit, the SS resistance R_1 can be approximated as given in Equation 3.5:

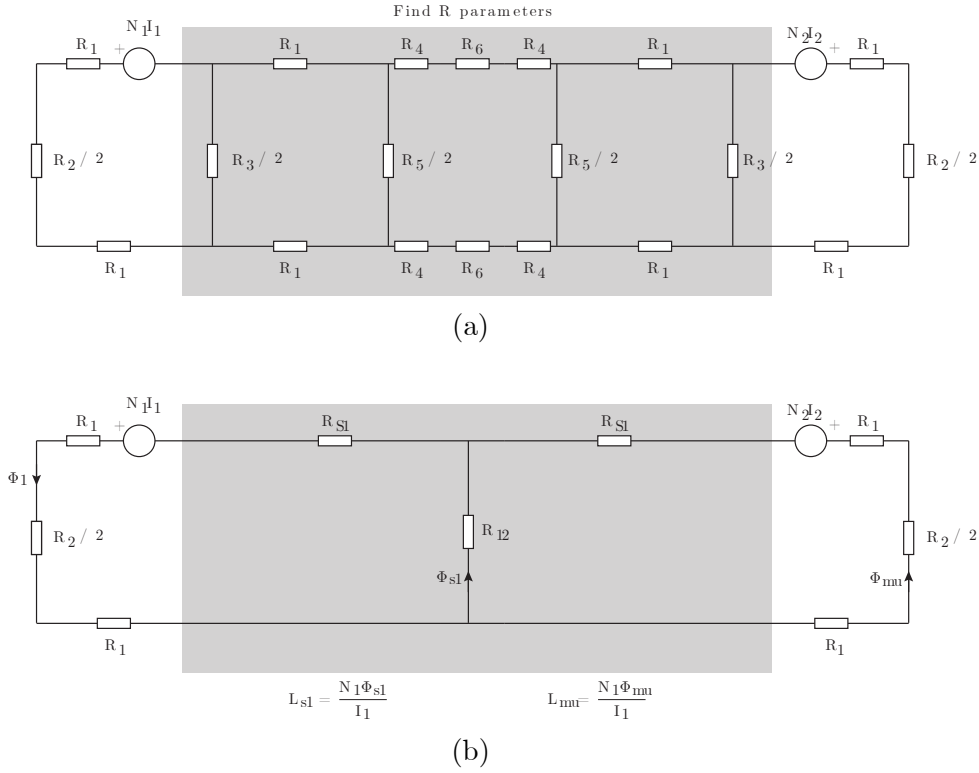


Figure 3.10: Reluctance network of OFC-WPT module:: **(a):** Reluctance network of simplified magnetic network (Figure 3.9(b)). The network in the shaded area is a typical ladder network, **(b):** The ladder network is reduced to T-network.

$$\left\{ \begin{array}{l} w_{ss} = g_{ps} + w_{ps} + \frac{t_c}{2} \\ l_1 = l_c \\ A_{ss} = t_{ss} \cdot w_{ss} \\ \therefore R_1 = \frac{l_1}{\sigma_{ss} A_{ss}} \end{array} \right. \quad (3.5)$$

where σ_{ss} is the conductivity of the SS, w_{ss} is the effective cross-sectional SS width, t_{ss} is the SS sheet thickness (0.5 mm thick SS sheets are used) and A_{ss} is the effective cross sectional area of the SS sheets for R_{SS} calculation.

For the region outside the slit, it is quite difficult to accurately calculate the path length taken by eddy currents. This path length can be approximated by arc from one side to other as shown in Figure 3.11. Moreover, the analytical model was verified in FEM an iteratively, a correction factor was used to match closely the value of R_{SS} from analytical calculations with the FEM based results. A closed form empirical result for R_2 is obtained

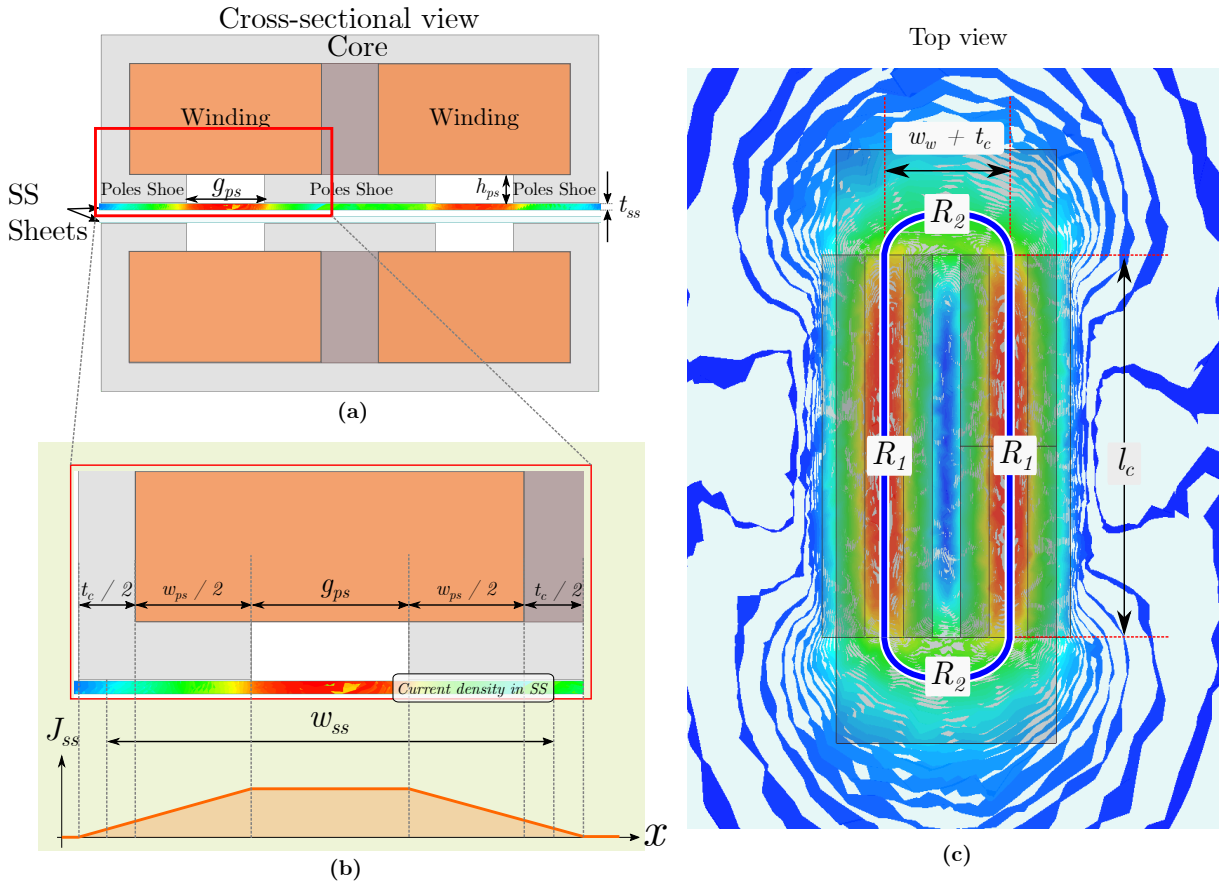


Figure 3.11: SS Resistance calculation

as in Equation 3.6:

$$\begin{cases} l_2 = 1.5 \cdot (w_w + t_c) \\ \therefore R_2 = \frac{l_2}{\sigma_{ss} A_{ss}} \end{cases} \quad (3.6)$$

Finally R_3 & hence R_{SS} can be calculated as in Equation 3.7:

$$\begin{cases} R_3 = 2 \cdot (R_1 + R_2) \\ \therefore R_{SS} = N_t^2 \cdot R_3 \end{cases} \quad (3.7)$$

The analytic model developed to calculate SS resistance however calculates the DC resistance and frequency dependent effects are neglected.

Frequency dependent AC winding resistance modeling

The conduction losses in the winding of OFC-WPT are modelled as equivalent winding resistance. The DC resistance of the windings can be straightforwardly calculated from the geometrical dimensions and winding material properties (Cu) as:

$$R_{w0,DC} = \frac{l_{Cu}}{\sigma_{Cu} A_w} \quad (3.8)$$

where $R_{w0,DC}$ is the single turn DC winding resistance, σ_{Cu} is the conductivity of the copper, $l_{Cu} = 2(2w_w + 2l_c + t_c)$ is the effective copper turn length, and A_w is the winding window area.

The total winding resistance for a N_t turn winding can be obtained as:

$$R_{w,DC} = N_t^2 \cdot R_{w0,DC} \quad (3.9)$$

However, for accurate calculation of Cu-losses, the high frequency effects need to be considered. The two main HF effects namely: *Skin* & *Proximity* effects need to be modelled to get the total AC losses. Thus, the AC resistance of the winding can be split into two components: $R_{w,AC-skin}$ & $R_{w,AC-prox}$. The calculation method of these are well established in the literature and in this thesis, one such method is used as described in [2] is used:

$$\begin{cases} R_{w,AC-skin} = R_{w,DC} \cdot 2F_R \\ R_{w,AC-prox} = R_{w,DC} \cdot 2G_R \cdot \left(\frac{H_{ext,RMS}}{I_{RMS}} \right)^2 \\ R_{w,AC} = R_{w,AC-skin} + R_{w,AC-prox} \end{cases} \quad (3.10)$$

The constants F_R & G_R depend mainly on geometrical parameters of winding and frequency and can be evaluated easily from the closed form expressions (see Appendix A.1). The main issue in calculating proximity effect comes to calculate the H-field distribution in the winding. The contribution of skin and proximity effect for each winding turn needs to be calculated individually and all the contributions need to be added finally to get the final AC resistance. For this, the H-field at each winding turn needs to be evaluated. The two methods used to evaluate H-field in FEM and analytical model are discussed below:

FEM Approach:

In FEM method, the winding is excited with 1A current and H-field is evaluated in a

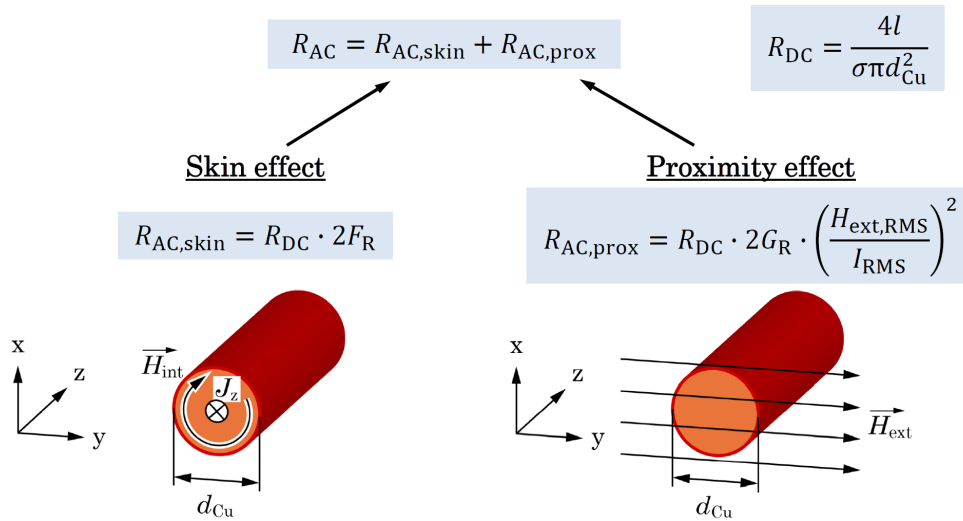


Figure 3.12: AC Winding resistance calculation methods [2].

3D-grid of discrete points inside the volume of winding post running the analysis, and the H-field data is exported to MATLAB. Figure 3.13 shows the distribution of H-field inside the winding section as indicated. Since the H-distribution is symmetric along the length of winding (along x -direction in Figure 3.13), it can be averaged along the axis of symmetry to give a 2D grid.

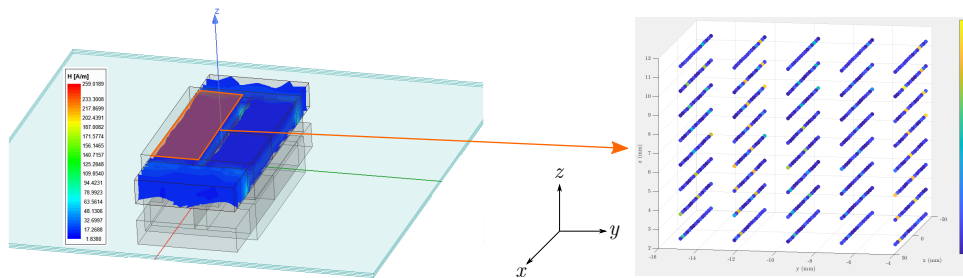


Figure 3.13: Extracting H-field data from FEM analysis.

For the section of winding lying inside of core, the H-field is symmetric along x -axis as shown in Figure 3.13, thus it can be averaged along x -axis to give us a 2D distribution of H-field in yz -plane. Then the H-field at the center of each winding turn can be interpolated and thus, proximity AC resistance can be calculated.

Analytic Approach:

In analytical method, the winding turns are assumed to be arranged in a rectangular fashion as shown in Figure 3.14 and 1A current is assumed to be flowing. Amperé’s Law can be used to calculate the H-field. Since the primary and secondary windings are not

on the same core, the Amperé's law is used in two directions and H-field is calculated for each layer. The individual contribution of the H-field for each turn is vectorially added so we can evaluate the AC proximity resistance.

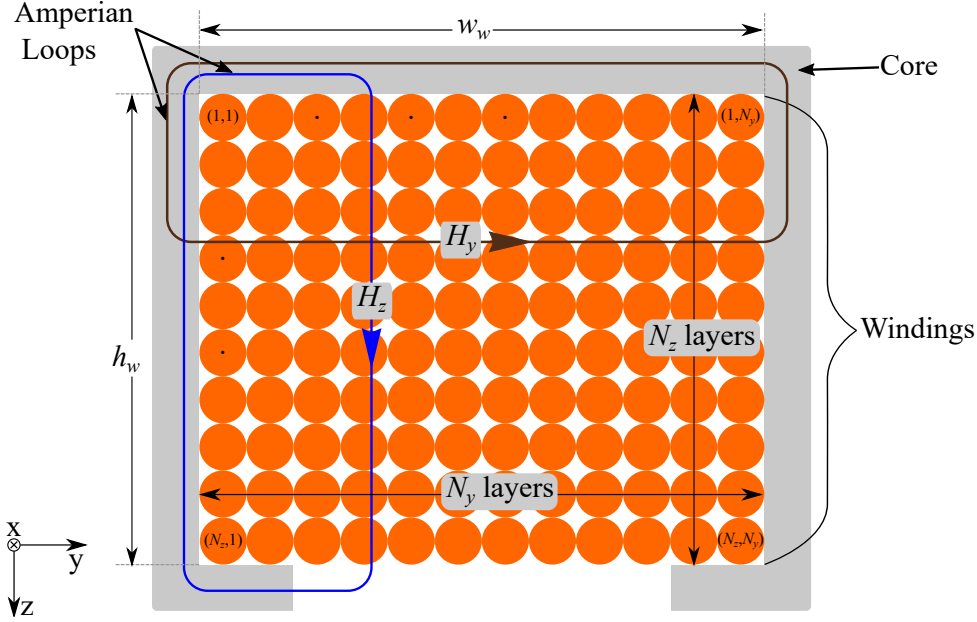


Figure 3.14: Analytical method of calculating H-field

For each layer in z and y direction, we can apply Amperé's law. The H-field inside the magnetic material is zero and thus H-field exists only in the region of winding. Thus, H-field in z and y can be calculated as:

$$\begin{cases} (H_y)_{n_y} = \frac{N_t \cdot I_{rms}}{w_w} \cdot \frac{n_y}{N_y} \\ (H_z)_{n_z} = \frac{N_t \cdot I_{rms}}{h_w} \cdot \frac{n_z}{N_z} \end{cases} \quad (3.11)$$

where n_z is the layer number in z -direction, and it takes the values from $\{1 \text{ to } N_z\}$, n_y is the layer number in y -direction, and it takes the values from $\{1 \text{ to } N_y\}$. For each conductor at position (n_z, n_y) , the H-field can be calculated as:

$$H_{zy} = \sqrt{H_z^2 + H_y^2} \quad (3.12)$$

Since $I_{rms} = 1A$ & $N_t = N_z \cdot N_y$, we can rewrite Equation 3.11 as:

$$\begin{cases} (H_y)_{n_y} = \frac{N_z}{w_w} \cdot n_y \\ (H_z)_{n_z} = \frac{N_y}{h_w} \cdot n_z \end{cases} \quad (3.13)$$

3.3. Geometry Optimization

In previous section we have seen how we can obtain the model parameters for optimization. The main aim for optimization is to find the best parameters which would give the most optimum performance. This thesis mainly focuses on the geometry optimization of OFC-WPT to achieve best efficiencies. However, as we saw in Section 3.2, since there are too many parameters involved, it is very difficult to interpret the pareto results. Thus, boxed volume optimization approach is used. Figure 3.15 shows the concept of boxed volume optimization.

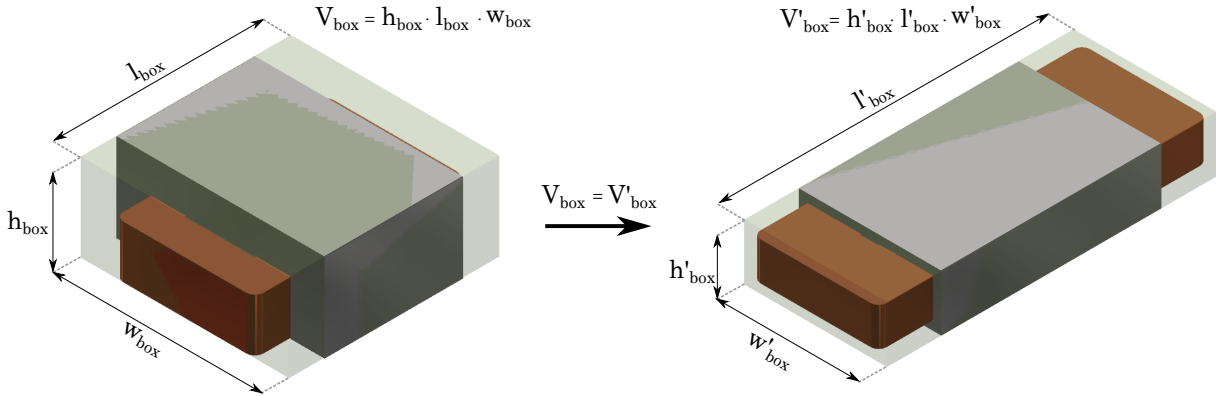


Figure 3.15: Box Optimization: The boxed volume of inductor is constant, while other geometrical parameters are varied.

The overall boxed volume of the inductor (including core and winding) is kept constant and the other geometrical parameters are varied. In addition to keeping the box volume constant, the output power and input voltage is also kept constant. Thus the module is optimized for constant 50W output power at fixed 60V input voltage. The optimization variables are therefore:

- Operational parameters: f_{sw}, R_{Load}
- Constructional parameters: N_t
- Geometrical Parameters ($l_c, w_c, t_c, h_c, g_{ps}, \dots$)

For the purpose of optimization, the analytical approach is used. To keep the power con-

stant at 50W, the load resistance needs to be calculated according to the circuit parameters. Once model parameters are calculated, the network is simplified to a Thevenin's Equivalent and for a constant 50W, the load resistance R_{Load} is calculated (See Appendix A.2). The workflow of the analytical method is shown in Figure 3.16.

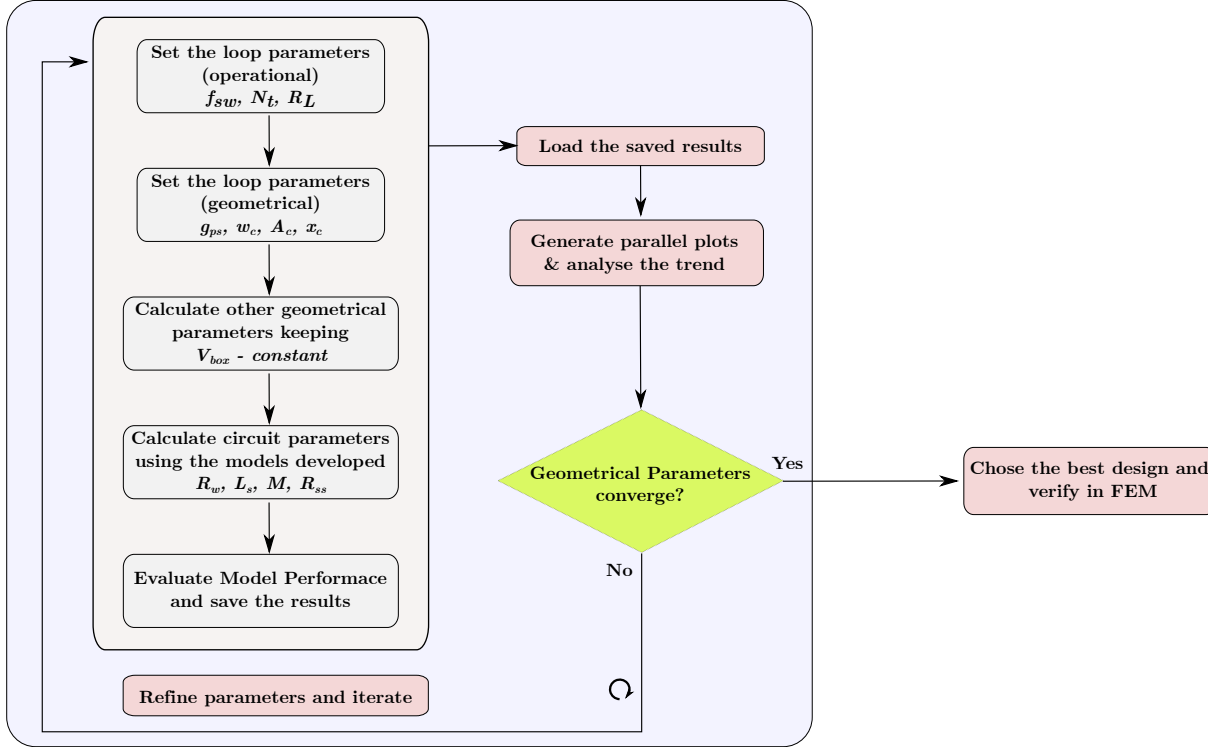


Figure 3.16: Analytical method of Optimization Flowchart

Some optimization constraints are kept to filter out the invalid design. These are:

- Peak Flux density inside the core $\leq 0.3 T$ (typical value for ferrite cores)
- Wire diameter $\leq 1 mm$ (for easy winding on coil former)

Since the volume and output power are kept constant, the power density is therefore constant. Therefore, the $\eta - \rho$ pareto plot would be just a straight line. Therefore, it is not a very convinient way to interpret the optimization results. Thus, the optimization results are plotted on a parallel-coordinate plot as shown in Figure 3.17 & 3.18. The base design is added along with all the other valid design in Figure 3.17 for comparison with the base design. Figure 3.18 shows all the valid design without the base designs.

Optimization Result interpretation:

The Optimization trend can be seen in Figure 3.18. Since the optimization is done for constant volume and power, the most efficient desgin can be chosen. The optimized design

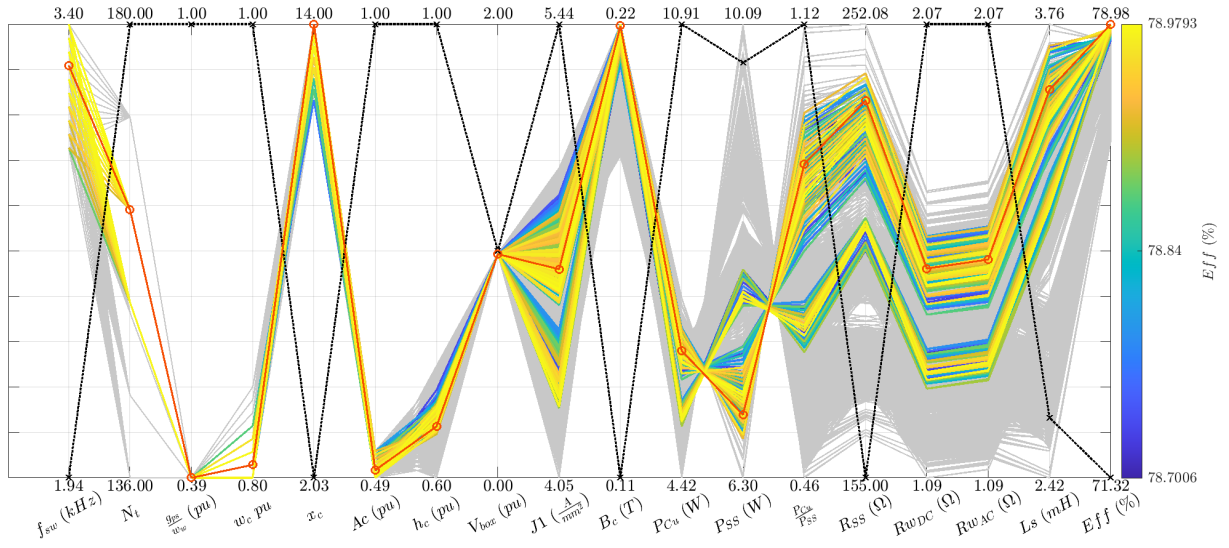


Figure 3.17: Parallel coordinate plot with base design included. The base design is highlighted in black, while chosen design is highlighted in orange. Designs not meeting filtering criteria are greyed out

is also highlighted on the plot. From the trend, the following conclusions can be made:

- Higher core aspect ratio (x_c) design tends to be more efficient. This is because higher $x_c \implies$ higher l_c . Since the SS resistance (R_1 , ref Eqn. 3.5) depends directly on l_c , $\therefore x_c \uparrow \implies R_{SS} \uparrow \implies SS \text{ Losses } (P_{SS}) \downarrow$.
- Increasing x_c i.e. increasing l_c & reducing t_c , means that w_c and h_c needs to be reduced to keep the boxed volume constant. However, reducing w_c have effect on reducing the winding width w_w (and increasing the area $l_c h_w$). This results in reducing the leakage reluctance R_3 (ref Table 3.2). This will increase the leakage inductance (L_σ). Due to this, the mutual flux decreases and to transmit same power, we need more total flux. Thus, saturation of the core occurs. Therefore there is an optimum x_c or l_c .
- w_c will reduce due to increase in l_c , but since it cannot be too small to avoid increase in leakage flux, thus there is an optimum w_c . And since box volume (V_{box}) is constant, \therefore there is optimum h_c as well.
- The core limb thickness t_c can be reduced due to the fact that the peak flux density in base design was ≈ 0.15 T. Increasing x_c allows us to reduce t_c and therefore reducing core cross sectional area A_c . This was we can operate the module closer to the saturation value and we can better utilize the core material. Further, since \hat{B} depends on applied voltage (\hat{U}_{in}), number of turns (N_t), switching frequency

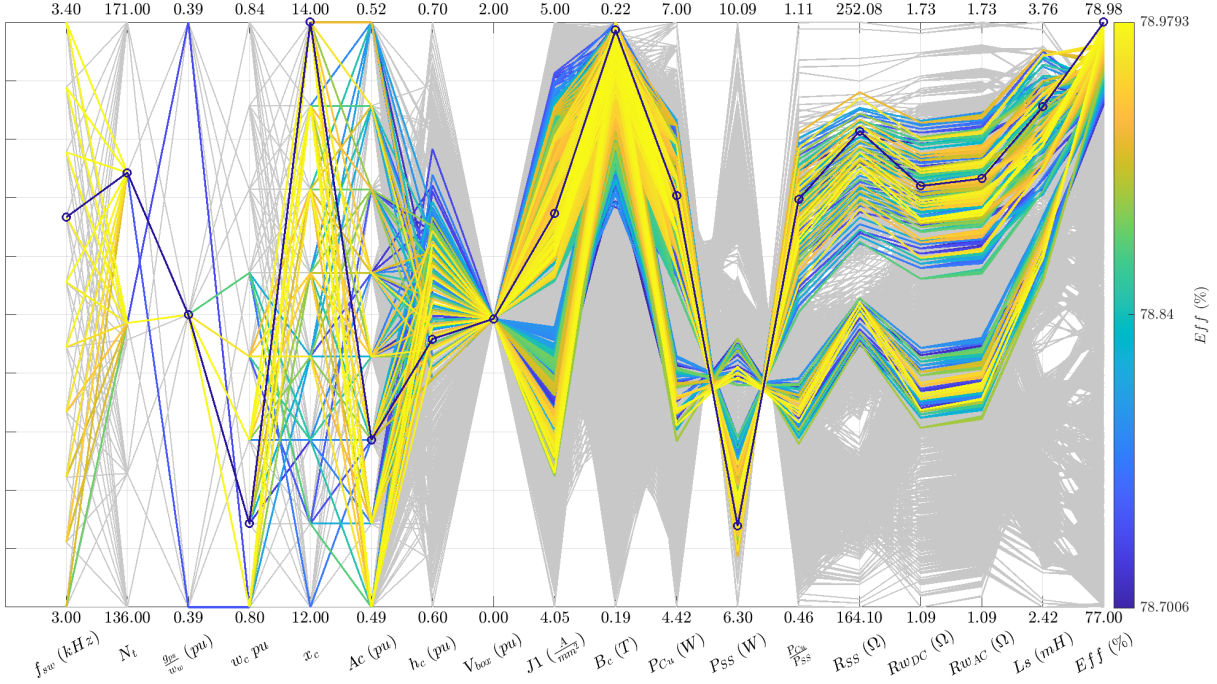


Figure 3.18: Parallel coordinate plot without base design included. The chosen design is highlighted in Blue. The invalid designs are greyed out.

(f_{sw}) and on A_c , reducing A_c allows us to operate at higher switching frequencies. However, higher switching frequencies also increases AC losses in the windings, \therefore we have an optimum f_{sw}

- Reducing t_c has effect on increasing the effective winding window area ($A_w = w_w h_w$). This allows to reduce the winding resistance and hence reduce copper losses (P_{Cu}). However, increase in l_c increases the winding length, which increases the winding resistance. Thus we have an optimum l_c and $\therefore A_w$.
- Since R_{SS} depends on N_t^2 , higher N_t is desirable. But, higher $N_t \implies$ higher R_w & L_σ . This also have effect in increasing the \hat{B} in the core. Thus, there is an optimum N_t .
- Further, the introduction of pole shoes have allowed us to reduce the effective cross section of the SS sheets (A_{ss} , see Eqn 3.5). Lower g_{ps} is desirable to reduce w_{ss} and thus increase R_{SS} . However, reducing g_{ps} would lead to reduction in reluctance R_5 (see Table 3.2), and increasing the leakage flux. Therefore, there is also an optimum g_{ps} .

Figure 3.19 shows the comparison of efficiencies and losses in the module evaluated by analytical and FEM method for the optimized design:

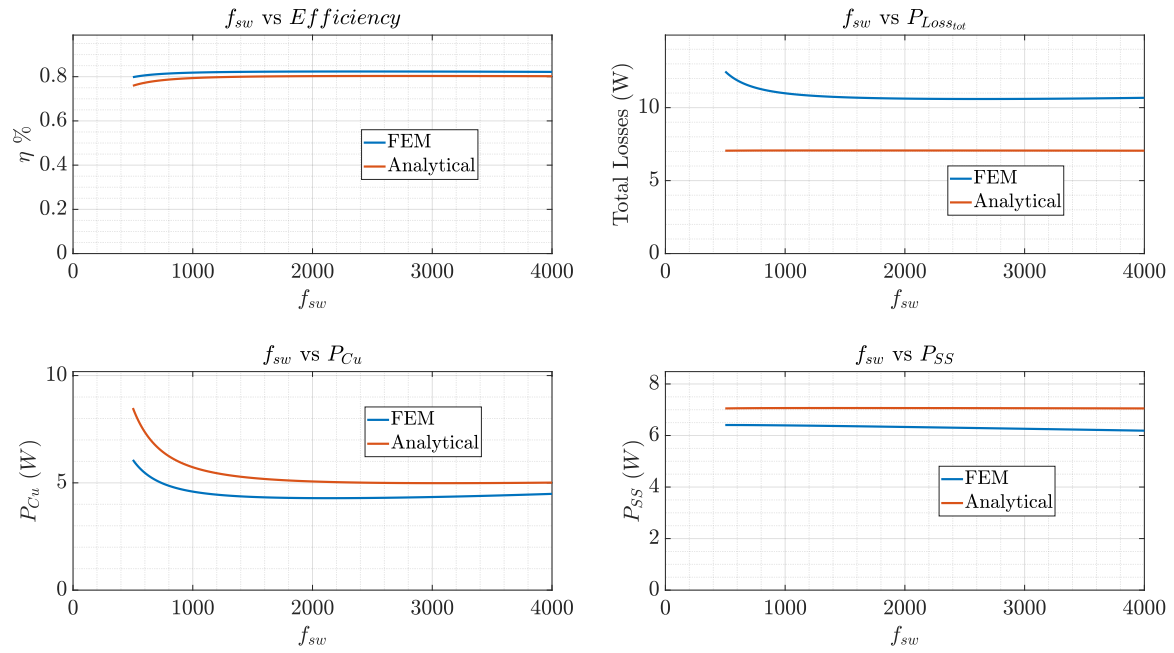


Figure 3.19: Efficiency and Loss plots for the OFC-WPT calculated through analytical and FEM methods

As can be seen, the Analytical model matches closely the trend of FEM output.

4 | Hardware Implementation

After optimization is done, the best design is chosen. The performance is verified in FEM and then actual module in hardware is to be realized. In this chapter we will see the realization of WPT module. We would also look at the consideration of effect of coil former on the reduction of winding window area and thus effect on performance. Later, we will see the Power Electronics realization for the WPT module.

4.1. WPT Hardware Realization

4.1.1. Analysis of Optimisation optimum design

In the Section 3.3 we had seen the optimization of OFC-WPT module using analytical approach. We also saw the interpretation of the optimization results and based on the results, we chose the highest efficiency design. The optimized design geometry with optimized geometrical dimensions is shown in Figure 4.1. The module is expected to operate of 78.9% efficiency. The analytical calculations of the module are verified by modelling it in FEM environment. Table 4.1 shows the comparison of the results obtained from FEM as well as Analytical approach.

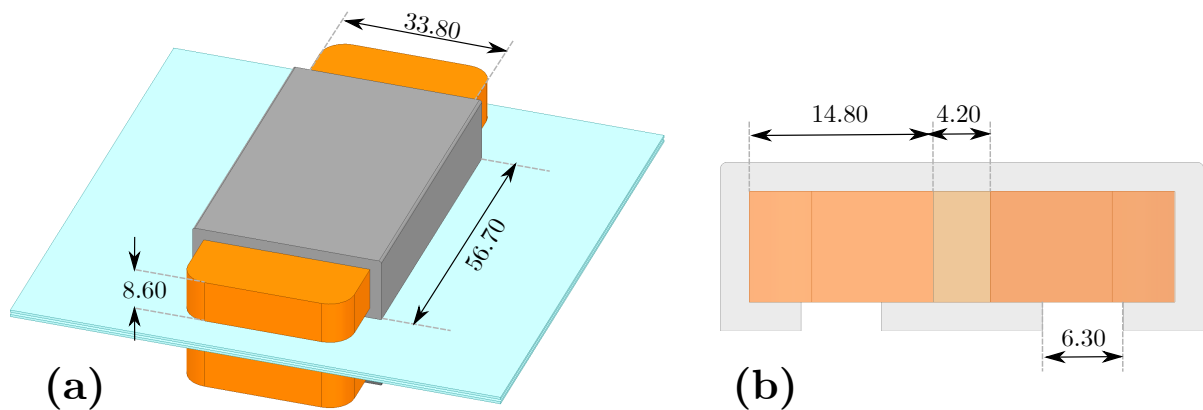


Figure 4.1: Physical dimensions of the optimized design:: (a): 3D view, (b): Cross-sectional view. (All dimensions are in *mm*).

Parameters	FEM Analysis Result	Analytical results	% Error
R_w (Ω)	1.28	1.65	22.03
L_s (mH)	4.25	3.90	-8.85
M (mH)	9.75	7.80	-25.00
R_{SS} (Ω)	273.60	238.60	-14.67
P_{in} (W)	75.99	63.66	-19.37
P_{out} (W)	62.77	50.00	-25.54
P_{SS} (W)	6.78	6.68	-1.5
P_{Cu} (W)	6.12	6.77	-9.6
P_{Core} (W)	0.24	0.21	-12.38
η (%)	82.60	78.53	-5.18
K_{coup}	0.62	0.60	-1.83

Table 4.1: Comparison of FEM and Analytical results for the optimized design.

As can be seen, the results from FEM and analytical approach matches quite closely.

4.1.2. WPT Module realization

To realize the optimized design module, a custom made ferrite E-core was required. However, it was quite expensive to manufacture, hence the model was realized with small ferrite I-cores as building blocks.

The main E-core is assembled on a 3D-printed structure and the I-core are glued together to make the main E-core structure except the central limb. The central limb is inserted in the coild former and the winding and coil former is inserted in E-core structure to complete the E-core module.

The pole shoes are glued to the bottom of coil former to complete the assembly.

Figure 4.2 shows the 3D render of the actual model and Figure 4.3 shows the actual assembly.

4.2. Power Electronics for WPT

The WPT module is to be supplied by a Power Electronic converter system. Most common topology used for IPT applications is isolated DC-DC converters [3], Figure 4.4 shows the

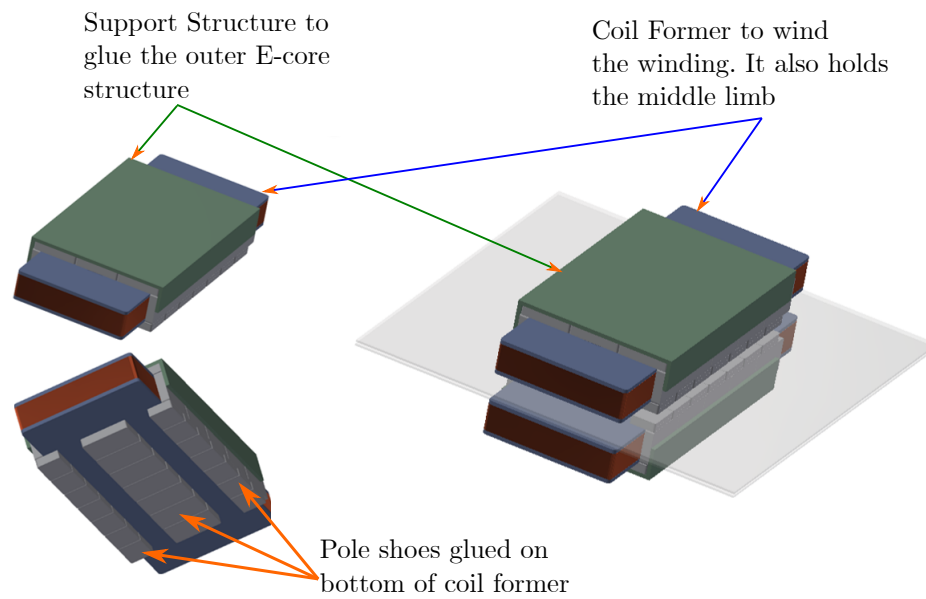


Figure 4.2: 3D-render of OFC-WPT module

topology of a typical isolated DC-DC converter system applied to IPT systems. The primary side is supplied through a $1 - \phi$ inverter while the receiving side is a diode bridge. The Primary side converter was realized using two Half bridges in H-bridge configurations. Existing MALTA board was used to realize the converter system. TI F28069M board was utilized to generate the PWM signals. Figure 4.5 shows the realized converter on PCB.

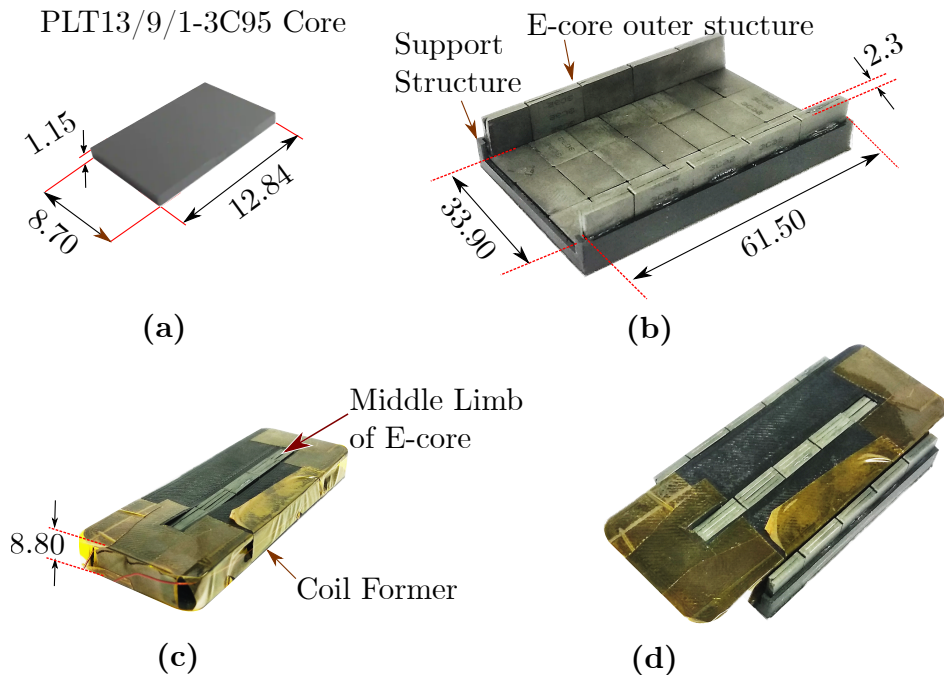


Figure 4.3: Actual assembly of OFC-WPT:: (a): I-core, (b): Outer structure of E-core glued on a 3D printed support structure, (c): Winding wound on a 3D printed coil former and middle limb of E-core inserted in the slot, (d): Coil shown in (c) is inserted in the E-structure shown in (b). Finally pole shoes are glued to the bottom of coil former to complete the assembly. (All dimensions are in mm)

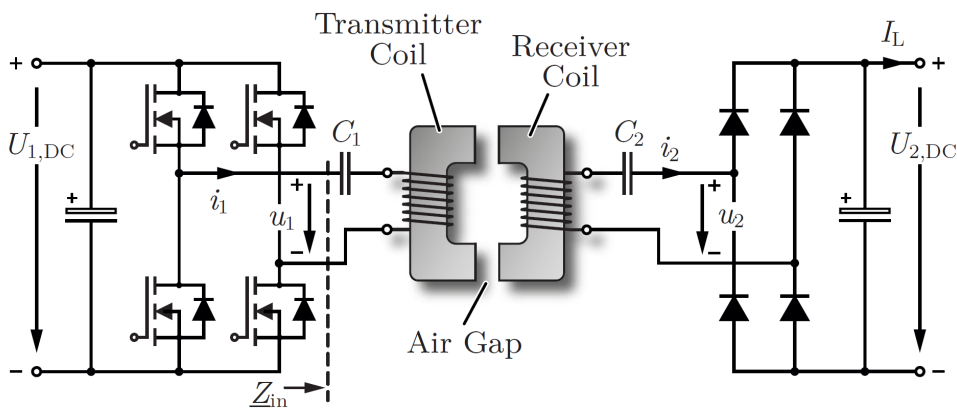


Figure 4.4: PE-converter topology for WPT applications [3]

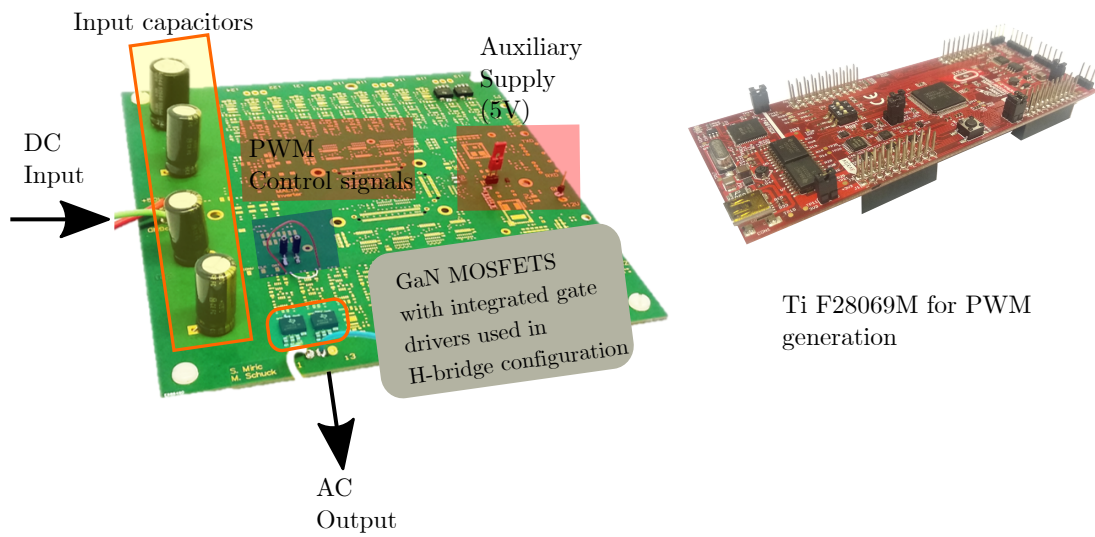


Figure 4.5: PE-converter for OFC-WPT

5 | Results

Till now the complete modelling process and optimization methodologies adopted were discussed. Based on the optimization results, the most optimum design was selected and realized in hardware. In this chapter, the discussion is further extended with the tests performed on the module, and finally, analytic, FEM as well as measure data is compared.

5.1. Measurement Techniques

From FEM, the standard method to evaluate circuit parameters is to setup frequency sweep analysis using current based excitation, which directly gives the Z-parameters of the module. Once Z-parameters are known, the circuit parameters can be easily calculated from Equation set 2.8.

However, on real system, it is not very intuitive to obtain Z-parameters Z_{11} , Z_{12} , Z_{21} , Z_{22} . To obtain circuit parameters, the Open-Circuit (Z_{OC}) and Short-Circuit (Z_{SC}) Impedances can be measured, and based on that, the Z-parameters can be calculated.

For an ideal transformer which has been simplified for a general transformation ratio $n = k\sqrt{L_1/L_2}$ (ref. Figure 2.2(c)), the Leakage (L_σ) & Mutual (L_μ) can be evaluated by OC and SC tests as shown in Figure 5.1. [3]

For determining L_σ , the secondary winding is short-circuited and primary is excited with a sinusoidal voltage having angular frequency ω . By measuring the current i_1 , the leakage inductance can be calculated as shown in Equation 5.1:

$$L_\sigma = \frac{\hat{U}_1}{\omega \hat{I}_1} \Big|_{u_2=0} \quad (5.1)$$

Similarly, for calculating L_μ , the secondary side is left open while supplying the primary side. The voltage measured on secondary side gives us the magnetizing inductance (Equation 5.2): [3]

$$L_\mu = \frac{\hat{U}_2}{\omega \hat{I}_1} \Big|_{i_2=0} \quad (5.2)$$

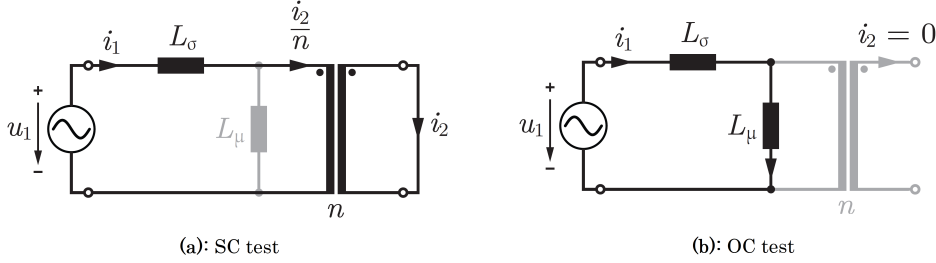


Figure 5.1: OC & SC tests on ideal transformer to determine L_σ & L_μ . [3]

Similar approach can be extended to real transformer. For our purpose, the impedance measurement is done by a Bode Analyzer, and the system is swept for different frequencies to capture its impedance over entire frequency range. Looking at our equivalent circuit of OFC-WPT (ref. Figure 2.8), the OC and SC measurement setup would look as shown in Figure 5.2.

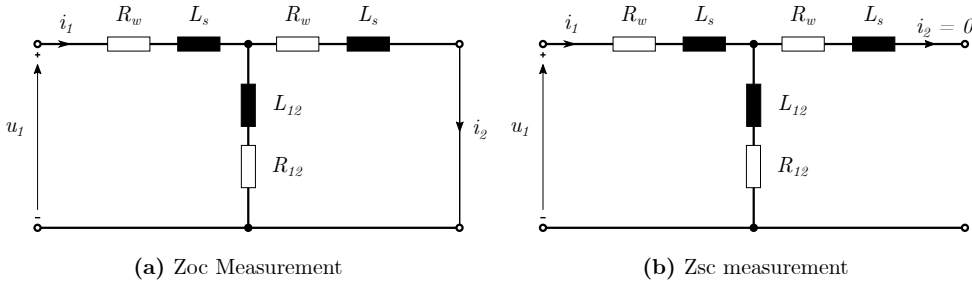


Figure 5.2: SC & OC measurement on OFC-WPT

Looking at Figure 5.2, we can define some impedances as:

$$\begin{aligned} \underline{Z}_s &= R_w + j\omega L_s \\ \underline{Z}_{12} &= R_{12} + j\omega L_{12} \\ \underline{Z}_{11} &= \underline{Z}_{22} = \underline{Z}_s + \underline{Z}_{12} \end{aligned} \quad (5.3)$$

From SC and OC measurements we would measure the impedances $Z_{OC} = R_{OC} + j\omega L_{OC}$ & $Z_{SC} = R_{SC} + j\omega L_{SC}$. These impedances can be related to the impedances defines in Equation 5.3 as shown in Equation 5.4:

$$\begin{aligned} \underline{Z}_{SC} &= \underline{Z}_s + (\underline{Z}_s || \underline{Z}_{12}) \\ \underline{Z}_{OC} &= \underline{Z}_s + \underline{Z}_{12} \end{aligned} \quad (5.4)$$

From Equations 5.3 & 5.4, we can write that:

$$\begin{aligned} \underline{Z}_{11} &= \underline{Z}_{OC} + \underline{Z}_{SC} \\ \underline{Z}_{12} &= \sqrt{(\underline{Z}_{11} - \underline{Z}_{SC}) \cdot \underline{Z}_{11}} \end{aligned} \quad (5.5)$$

Thus, once \underline{Z}_{11} & \underline{Z}_{12} are known from Equation 5.5, \underline{Z}_s can be calculated as $\underline{Z}_s = \underline{Z}_{11} + \underline{Z}_{12}$. And once \underline{Z}_s & \underline{Z}_{12} are known, the circuit parameters R_w , L_s , M & R_{SS} can be calculated.

5.2. Prototype Testing

The WPT module realized in Section 4.1.2 is tested to observe the performance. Figure 5.3 shows the Impedance data obtained from a SC and OC measurement made on the realized WPT module:

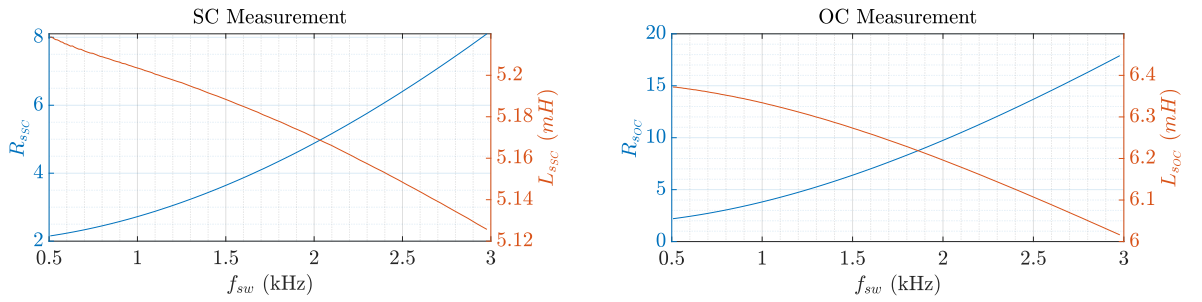


Figure 5.3: SC and OC measurement from Impedance Analyzer

Based on the Obtained SC and OC data, we can calculate the parameters as we had seen in Section 5.1. The plots of calculated parameters are shown in Figure 5.4:

Based on the circuit parameters calculated from Impedance measurements, the performance of the OFC-WPT was evaluated. The performance trend can be seen in Figure 5.5. It can be seen that the efficiency of the module has increased from 72 % upto 84%.

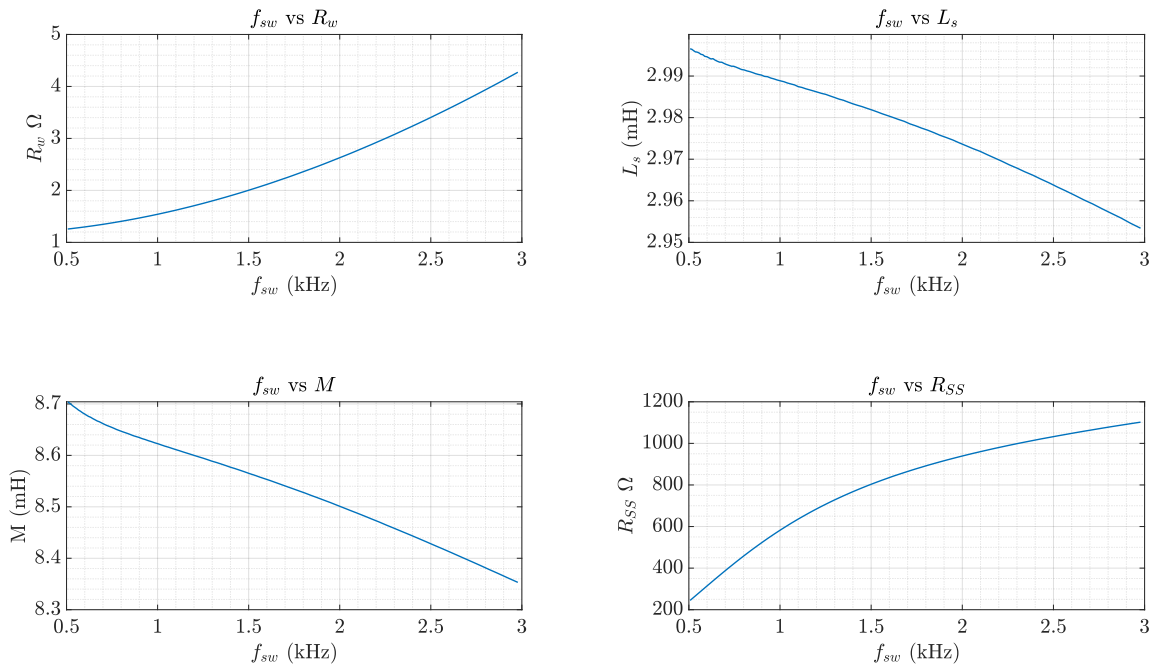


Figure 5.4: Circuit parameters of OFC-WPT module calculated from Impedance Analyzer measurement.

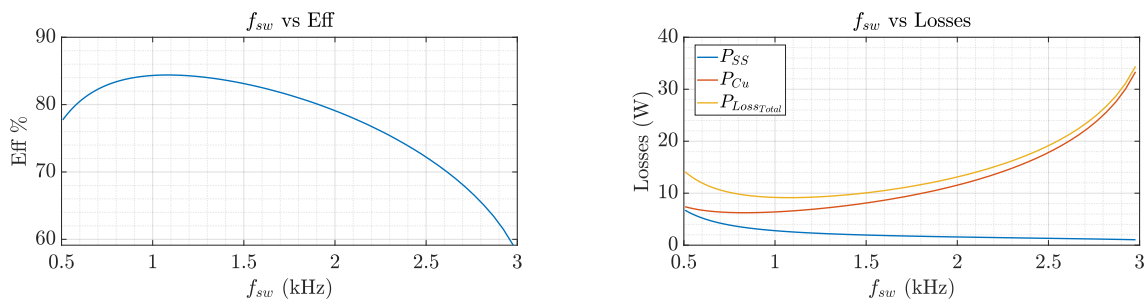


Figure 5.5: Efficiency and Loss plots for the OFC-WPT measurement data. The model has achieved an efficiency of $\approx 84\%$ while reducing the losses in SS as well as copper.

6 | Conclusion

6.1. Outlook

This thesis presented the optimization of the OFC-WPT module, developing analytical model and performing constant boxed volume optimization. The effect of different geometrical parameter was observed on the circuit parameters, such as on SS resistance (R_{SS}), winding resistance (R_w), Leakage and Mutual inductances (L_σ & M), and on performance parameters such as N_t , f_{sw} , power losses, coupling factors etc. These observations were used to further refine the course of optimization.

The optimization resulted in a OFC-WPT module giving us $\approx 84\%$ efficiency for same volume and input voltage. The optimized geometrical parameters allowed us to increase the R_{SS} from 155Ω in base design to 635Ω and hence reducing P_{SS} to 3W, reduce R_w from 2Ω to 1.6Ω hence reducing P_{Cu} to 6W and reducing total losses to 9W. The optimized design is also operated at higher frequencies and with lower core cross sectional area, hence operating it near the knee on magnetic curve, thus utilizing the magnetic material better.

Finally the optimized design was developed in hardware and the results were verified by testing and measurements.

6.2. Future Work

Since many of the parameters of the OFC-WPT were kept constant during the optimization (such as volume, input voltage, output power), there are opportunities to further improve the performance by also incorporating these parameters for optimization. Further, the scaling laws for such OFC-WPT modules can be developed to design them for higher power ratings.

Bibliography

- [1] A. Abdolkhani. Fundamentals of inductively coupled wireless power transfer systems. In E. Coca, editor, *Wireless Power Transfer*, chapter 1. IntechOpen, Rijeka, 2016. doi: 10.5772/63013. URL <https://doi.org/10.5772/63013>.
- [2] J. Biela. *Optimierung des elektromagnetisch integrierten Serien-Parallel Resonanzkonverters mit eingepprägtem Ausgangsstrom*. PhD thesis, ETH Zürich, 2005.
- [3] R. Bosshard. *Multi-Objective Optimization of Inductive Power Transfer Systems for EV Charging*. PhD thesis, ETH Zürich, 2015.
- [4] R. Bosshard, U. Badstübner, J. W. Kolar, and I. Stevanović. Comparative evaluation of control methods for inductive power transfer. In *2012 International Conference on Renewable Energy Research and Applications (ICRERA)*, pages 1–6, 2012. doi: 10.1109/ICRERA.2012.6477400.
- [5] R. Bosshard, J. W. Kolar, J. Mühlethaler, I. Stevanović, B. Wunsch, and F. Canales. Modeling and $\eta - \alpha$ pareto optimization of inductive power transfer coils for electric vehicles. *IEEE Journal of Emerging and Selected Topics in Power Electronics*, 3(1): 50–64, 2015. doi: 10.1109/JESTPE.2014.2311302.
- [6] T. Guillod and J. W. Kolar. Medium-frequency transformer scaling laws: Derivation, verification, and critical analysis. *CPSS Transactions on Power Electronics and Applications*, 5(1):18–33, 2020. doi: 10.24295/CPSSTPEA.2020.00003.
- [7] T. Guillod, F. Krismer, and J. W. Kolar. Magnetic equivalent circuit of mf transformers: modeling and parameter uncertainties. *Electrical Engineering*, 100(4):2261–2275, 2018.
- [8] S. Mirić, M. Tatić, J. Huber, D. Bortis, and J. W. Kolar. “pushing power through walls” - wireless power transfer through stainless steel. In *2021 24th International Conference on Electrical Machines and Systems (ICEMS)*, pages 743–751, 2021. doi: 10.23919/ICEMS52562.2021.9634258.

- [9] J. Mühlethaler. *Modelling and Multi-Objective Optimization of Inductive Power Components*. PhD thesis, ETH Zürich, 2012.
- [10] M. Tatić. Wireless power transfer through stainless steel. Master's thesis, ETH Zürich, 11 2021.
- [11] Z. Zhang, H. Pang, A. Georgiadis, and C. Cecati. Wireless power transfer—an overview. *IEEE Transactions on Industrial Electronics*, 66(2):1044–1058, 2019. doi: 10.1109/TIE.2018.2835378.

A | Appendix A

A.1. Equations for AC constant calculations

$$F_R(f) = \frac{\xi}{4\sqrt{2}} \left[\frac{\text{num}_{FR}(\xi)}{\text{Br}_1(\xi)^2 + \text{Bi}_1(\xi)^2} \right]$$

$$\text{num}_{FR}(\xi) = \text{Br}_0(\xi)\text{Bi}_1(\xi) - \text{Br}_0(\xi)\text{Br}_1(\xi) - \text{Bi}_0(\xi)\text{Br}_1(\xi) - \text{Bi}_0(\xi)\text{Bi}_1(\xi)$$

$$G_R(f) = -\frac{\xi\pi^2 d^2}{2\sqrt{2}} \left[\frac{\text{num}_{GR}(\xi)}{\text{Br}_0(\xi)^2 + \text{Bi}_0(\xi)^2} \right],$$

$$\text{num}_{GR}(\xi) = \text{Br}_2(\xi)\text{Br}_1(\xi) + \text{Br}_2(\xi)\text{Bi}_1(\xi) + \text{Bi}_2(\xi)\text{Bi}_1(\xi) - \text{Bi}_2(\xi)\text{Br}_1(\xi)$$

$$\xi = \frac{d}{\sqrt{2}\delta} \quad \text{and} \quad \delta = \frac{1}{\sqrt{\pi\mu_0\sigma f}},$$

A.2. Load Resistance calculation for constant 50W output power

To calculate the load resistance for giving constant output power for varying circuit parameter, the thevenin's approach can be used.

The OFC-WPT simplified equivalent circuit as shown in Figure 2.8(b), the Thevenin's equivalent voltage u_{th} and Thevenin's Impedance Z_{th} can be evaluated as:

$$\begin{aligned} \underline{Z}_{th} &= R_w + (\underline{Z}_{12} || R_w), \quad \& \\ u_{th} &= u_1 \cdot \frac{\underline{Z}_{12}}{\underline{Z}_{12} + R_w} \end{aligned} \tag{A.1}$$

Once u_{th} and Z_{th} are known, then it can be used to calculate load resistance R_L such that

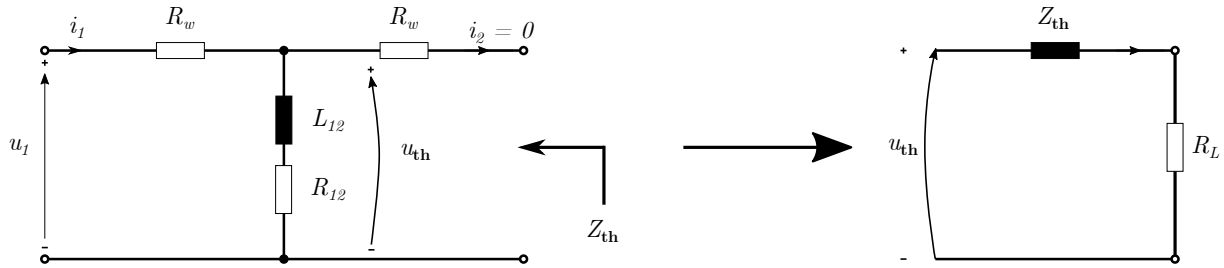


Figure A.1: Thevenin's Equivalent Impedance and Voltage calculation

the source u_{th} delivers required power (50W) in our case.

$$i_2 = \frac{u_{th}}{Z_{th} + R_L}, \quad \& \quad (A.2)$$

$$P_o = 0.5 \cdot |i_2|^2 \cdot R_L$$

Then just solve for R_L such that $P_o = 50W$

List of Figures

1.1	Previous Work on OFC-WPT [8]	2
2.1	Elements of Inductively Coupled WPT system [1]	5
2.2	Equivalent circuit of an ideal transformer: (a) : Ideal transformer with $n = 1$, (b) : Ideal transformer with $n \neq 1$, (c) : Ideal transformer with $n = k\sqrt{L_1/L_2}$; [3]	7
2.3	Equivalent circuit of an a real transformer including loss components. [8] .	8
2.4	WPT Concepts through SS: (a) : Orthogonal Field Concept (OFC) - \vec{B} & SS sheets are orthogonal, & (b) : Parallel Field Concept (PFC) - \vec{B} & SS sheets are parallel	9
2.5	Equivalent circuit model of OFC-WPT	10
2.6	Complete equivalent circuit of OFC-WPT through SS	11
2.7	Compensation Networks for IPT: (a) : Series-Series, (b) : Series-Parallel, (c) : Parallel-Series, & (d) : Parallel-Parallel. [11]	12
2.8	Series Compensated Equivalent circuit of OFC-WPT	13
3.1	Induced EMF distribution for an E-core type OFC WPT module	16
3.2	Induced Eddy Current distribution for an E-core type OFC WPT module along the center line of SS sheets.	17
3.3	Pole Shoe Types explored:: (a) : Pole Shoes placed at the center of each limb with equal pole width on each side, (b) : Pole shoes placed symmetrically to get symmetric gap between the pole shoes, (c) : Pole shoes placed on central limb to increase distance between air-gaps.	17
3.4	Geometrical Dimensions of OFC-WPT Module	18
3.5	FEM Optimization Flowchart	20
3.6	η - ρ Pareto Plot for FEM based optimization analysis, with filtering criteria applied as:- $\hat{B}_{pk} \leq 0.3T$, $d_{wire} \leq 1mm$, $\hat{J}_{pk} \leq 5A/mm^2$ & $\eta \geq 78\%$	21
3.7	FEM Workflow	22
3.8	Field Plots of FEM analysis:: (a) : Flux density distribution inside the core, (b) : Current density distribution inside the windings	23

3.9	Magnetic modelling of OFC-WPT module:: (a) : E-core split into different sections and reluctances calculated for for each section, (b) : Reluctance model simplified along the central symmetry axis.	24
3.10	Reluctance network of OFC-WPT module:: (a) : Reluctance network of simplified magnetic network (Figure 3.9(b)). The network in the shaded area is a typical ladder network, (b) : The ladder network is reduced to T-network.	26
3.11	SS Resistance calculation	27
3.12	AC Winding resistance calculation methods [2].	29
3.13	Extracting H-field data from FEM analysis.	29
3.14	Analytical method of calculating H-field	30
3.15	Box Optimization: The boxed volume of inductor is constant, while other geometrical parameters are varied.	31
3.16	Analytical method of Optimization Flowchart	32
3.17	Parallel coordinate plot with base design included. The base design is highlighted in black, while chosen design is highlighted in orange. Designs not meeting filtering criteria are greyed out	33
3.18	Parallel coordinate plot without base design included. The chosen design is highlighted in Blue. The invalid designs are greyed out.	34
3.19	Efficiency and Loss plots for the OFC-WPT calculated through analytical and FEM methods	35
4.1	Physical dimensions of the optimized design:: (a) : 3D view, (b) : Cross-sectional view. (All dimensions are in <i>mm</i>).	37
4.2	3D-render of OFC-WPT module	39
4.3	Actual assembly of OFC-WPT:: (a) : I-core, (b) : Outer structure of E-core glued on a 3D printed support structure, (c) : Winding wound on a 3D printed coil former and middle limb of E-core inserted in the slot, (d) : Coil shown in (c) is inserted in the E-structure shown in (b) . Finally pole shoes are glued to the bottom of coil former to complete the assembly. (<i>All dimensions are in mm</i>)	40
4.4	PE-converter topology for WPT applications [3]	40
4.5	PE-converter for OFC-WPT	41
5.1	OC & SC tests on ideal transformer to determine L_σ & L_μ . [3]	44
5.2	SC & OC measurement on OFC-WPT	44
5.3	SC and OC measurement from Impedance Analyzer	45

List of Figures	55
5.4 Circuit parameters of OFC-WPT module calculated from Impedance Analyzer measurement.	46
5.5 Efficiency and Loss plots for the OFC-WPT measurement data. The model has achieved an efficiency of $\approx 84\%$ while reducing the losses in SS as well as copper.	46
A.1 Thevenin's Equivalent Impedance and Voltage calculation	52

List of Tables

3.1	Description of Geometrical Dimensions	18
3.2	Parameter description for calculation of reluctance model.	25
4.1	Comparison of FEM and Analytical results for the optimized design.	38

Acronyms

Abbreviation	Description
AC	Alternating Current
Cu	Copper
DC	Direct Current
EMF	Electromotive Force
EV	Electric Vehicle
FEM	Finite Element Method
HEV	Hybrid Electric Vehicle
HF	High Frequency
ICWPT	Inductively Coupled Wireless Power Transfer
iGSE	Improved Generalized Steinmetz Equation
IPT	Inductive Power Transfer
KCL	Kirchhoff's Current Law
KVL	Kirchhoff's Voltage Law
MF	Medium Frequency
MMF	Magnetomotive Force
OC	Open Circuit
OFC	Orthogonal Field Concept
PFC	Parallel Field Concept
SC	Short Circuit
SE	Steinmetz Equation
SS	Stainless Steel
WPT	Wireless Power Transfer

Acknowledgements

Firstly, I would like to thank Prof. Dr. Roberto Perini for supporting me during my exchange period and also acting as supervisor at my home university, Politecnico di Milano. Prof. Perini had always showed up in my hour of need and ensuring that all my administrative affairs were dealt with ease.

This thesis was done at PES Lab, ETH Zürich. I would like to extend my sincere thanks to Prof. Dr. Johann W. Kolar for giving the opportunity to be at PES lab and work on my MSc thesis as an exchange student. The entire thesis period spent at PES was a life changing experience where I got to work on challenging and latest research work. This thesis helped me broaden my horizons and allowed me to think in creative ways to deal with a problem.

This experience would not have been possible without continuous support and supervision of Dr. Spasoje Mirić, who always helped whenever I was in doubt. He had always provided necessary resources necessary to complete the thesis. It would also not have been possible to be at PES without the support of Dr. Jonas Huber who gave me the opportunity work on this topic. Through this thesis, I had gained critical skills in the magnetic design, wireless power transfer and hardware realization & prototyping.

I would also like to the exchange office of Politecnico di Milano and ETH Zürich for ensuring a smooth stay throughout. I would like to thank Ms. Ms. Paola Scorza (PoliMi) and Celia Ferreira Goicoechea (ETH) for supporting and helping me during my thesis exchange. I would also like to thanks the PES sekretariat, Ms. Pisca Murantonio for her help in administrative affairs. I would thank all the wonderful people at PES (MA students, PhD students, Professors...) with whom I had very interesting conversations.

Finally, I would like to thank my family for always keeping my motivation high, and to my friends and colleagues for believing in me and keeping my spirit alive.

